System Identification of Flexible Aircraft: Lessons Learned from the X-56A Phase 1 Flight Tests

Jared A. Grauer*
NASA Langley Research Center, Hampton, Virginia, 23681

Matthew J. Boucher†
NASA Armstrong Flight Research Center, Edwards, California, 93523

The X-56A Multi-Utility Technology Testbed (MUTT) is a subscale airplane that was designed as an experimental flight research platform for improving aeroelastic modeling and control technologies. The Phase 1 flight tests, conducted from 2017 to 2019 at the NASA Armstrong Flight Research Center (AFRC), included 39 flights and approximately 1000 research maneuvers, some of which demonstrated stable closed-loop flight beyond the open-loop flutter speed. This paper summarizes the system identification effort to extract nondimensional stability and control derivatives from the flight test data for constructing aeroelastic models of the flight dynamics. Topics discussed include instrumentation, experiment design, model postulation and reduction, parameter estimation, and others. Throughout the paper, unique challenges for the identification of flexible aircraft, practical aspects of the analysis, and lessons learned are presented.

Nomenclature

a_x, a_y, a_z	=	accelerometer measurements, g
$\bar{c}$	=	mean aerodynamic chord, ft
g	=	gravitational acceleration, ft/s^2
$\mathbb{I}$	=	identity matrix
I_{yy}	=	pitch moment of inertia, slug-ft^2
j	=	imaginary number, = $\sqrt{-1}$
m	=	aircraft mass, slug
p, q, r	=	body-axis angular rates, rad/s
$\bar{q}$	=	dynamic pressure, lbf/ft^2
S	=	wing reference area, ft^2
s	=	Laplace variable
t	=	time, s
V	=	true airspeed, ft/s
V_f	=	flutter speed, ft/s
w_{ff}	=	full-fuel weight, lbf
X_T	=	body x-axis thrust force, lbf
α, β	=	air flow angles, rad
γ	=	flight path angle, rad
Δ	=	perturbation quantity
δ	=	control surface deflection, rad
ϕ, θ, ψ	=	Euler angles, rad
ω	=	frequency, rad/s

Subscripts

a, f	=	aft or fore
c, m, o	=	center, midspan, or outboard
l, r	=	left or right

Superscripts

$^{-1}$	=	matrix inverse
^{T}	=	transpose
†	=	complex conjugate transpose
$\dot{}$	=	time derivative

Acronyms

FTA	=	flight test aid
SFA	=	symmetric wing fore-aft
SP	=	short period
SW1B	=	1st symmetric wing bending
SW1T	=	1st symmetric wing torsion
SWL	=	symmetric winglet lateral

*Research Engineer, Dynamic Systems and Control Branch, MS 308, Associate Fellow AIAA.
†Research Engineer, Controls and Dynamics Branch, MS 4840D, Member AIAA.

I. Introduction

The X-56 Multi-Utility Technology Testbed (MUTT) is a fixed-wing airplane that was built as a subscale aeroelastic technology demonstrator by the Lockheed Martin Aeronautics (LM Aero) Company while under contract to the Air Force Research Laboratory (AFRL). The airplane conceptual design was influenced by previous experience with SensorCraft-type aircraft, which were subsonic, high-altitude airplanes designed for long-endurance flights. These mission profiles led to aircraft configurations having lightweight structures and significant aeroelastic stability challenges. The primary goal in designing the X-56 was to achieve a low-cost, modular, and remotely-piloted test aircraft for maturing aeroelastic modeling and control technologies, and for performing high-risk flight demonstrations [1, 2].

LM Aero conducted 8 flights with the X-56A during 2013 for calibration and system check out at the NASA Dryden Flight Research Center (DFRC), now called Armstrong Flight Research Center (AFRC). During these flights, the so-called "stiff" wing set was used, which unlike the more "flexible" wing sets, does not contain aeroelastic instabilities within the normal flight envelope. In 2014, AFRL transferred the X-56A with documentation to AFRC for further testing. NASA then designed non-proprietary control laws for this aircraft and in 2015 conducted an additional 8 flights with the stiff wing set, which were called the Phase 0 flight tests, to clear the flight envelope, gain experience with the aircraft, and validate the control laws. From 2017 to 2019, the Phase 1 campaign included 39 flights and around 1000 research maneuvers using one flexible wing set. These flights were used to expand the flight test envelope, validate the NASA-developed simulation model, gather data for system identification analyses, and test flight control laws for flutter suppression. Several maneuvers during these flights successfully demonstrated closed-loop flight beyond the flutter speed [3].

The data gathered for system identification analyses were used to extract nondimensional stability and control derivatives for the aircraft. These estimates were used to update and verify the aerodynamic simulation database and to construct linear state-space models about reference flight conditions. Because aeroelastic flight dynamics models [4] are of larger order and can involve many more inputs and outputs than traditional rigid-body flight dynamics models [5], many challenges were encountered during the system identification analysis of the Phase 1 flight data that are not typically encountered with less flexible aircraft.

Several published documents [6–12] detail various aspects of the system identification analysis for the X-56A. In this paper, the broader system identification analysis is summarized. Although some background material is provided, the discussion is focused on the unique challenges encountered with identifying models for flexible aircraft, as well as possible solution strategies, practical details of the analyses, and lessons learned during the Phase 1 flight tests.

This paper is organized as the following. Section II describes the X-56A aircraft and flight operations. Section III summarizes the in-vacuo structural dynamics model. Section IV details the instrumentation of the airplane. Section V discusses the experiment design for system identification. Section VI describes the aeroelastic flight dynamics model. Section VII discusses synchronization and kinematic compatibility of the data. Section VIII describes the parameter estimation of stability and control derivatives. Lastly, Section IX concludes the paper.

The analysis was conducted in MATLAB® using custom subroutines and the software package called System IDentification Programs for AirCraft (SIDPAC) [13], which is associated with Ref. [14]. Because the flight test data are currently ITAR-restricted, numbers in physical units are not given in this paper.

II. Aircraft and Flight Test Operations

The X-56A airplane is pictured in flight over AFRC in Fig. 1(a), and a three-view drawing is shown in Fig. 1(b). The tailless flying-wing aircraft has swept-back wings and large stationary winglets installed at the wing tips. The aircraft is modular in construction and consists of a center body and a wing set. Each of the two identical and interchangeable center bodies contains a fuel tank, on-board computer, fixed tricycle landing gear, and a ballistic parachute recovery system. Two turbojet engines are attached to the aft section of the upper fuselage. Left and right body flap control surfaces are along the trailing edge and adjacent to the interface between the wings and center body. There are four sets of wings: one stiff set and three identical flexible sets. The flexible wing sets were designed to exhibit an aeroelastic instability within the normal flight envelope of the aircraft. Water tanks housed within the wings provided the ability to alter the mass distribution and vibration characteristics during flight, but were not used. There are four independent control surfaces along the trailing edge of each wing. Between the throttles, body flaps, and wing flaps, there are 10 independent control effectors for the bare-airframe dynamics.

The airplane is flown remotely using a ground control station housed in a trailer. A pilot and co-pilot fly the aircraft with stick and rudder inceptors using an out-the-nose video stream overlaid with a heads-up display and digital cockpit instrumentation. The ground control station also includes a nonlinear simulation of the aircraft, which is useful for

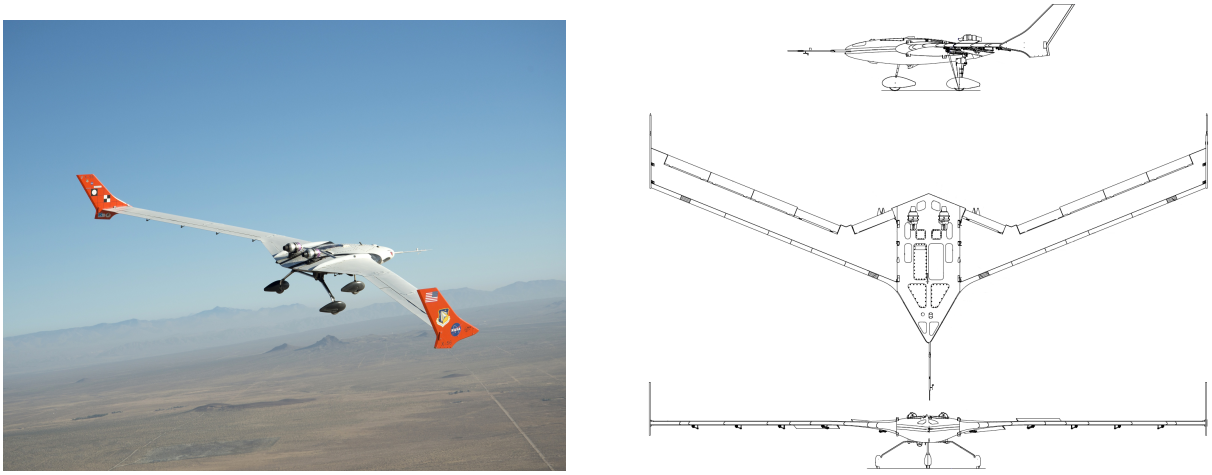

(a) Photograph (credit: NASA / Jim Ross).

(b) Three-view drawing.

Fig. 1 The X-56A airplane.

training and rehearsal, maneuver development, and hardware-in-the-loop simulation. Additional information on the aircraft, facilities, and flight operations can be found in Refs. [1, 2].

III. Structural Dynamics

The in-vacuo structural vibrations of the aircraft were characterized by a finite element model (FEM). The FEM contains natural frequencies, ω_i, and three-dimensional mode shapes (translational and rotational displacement vectors $\boldsymbol{\phi}_i^P$ and $\boldsymbol{\nu}_i^P$, respectively) for 25 vibration modes. The mode numbers are denoted by the subscript i. The FEM is tabulated for 17 fuel weight conditions between empty and full fuel weight (w_{ff}), and the mode shapes are spatially discretized over 8480 node points, which are denoted by the superscript P. The mode shapes were normalized so that the generalized masses m_i were equal to unity. A ground vibration test (GVT) was conducted at AFRC, which provided the modal damping ratios ζ_i at empty fuel and full fuel conditions, as well as other experimental data to which the FEM was tuned. See Refs. [15, 16] for more information on the FEM, GVT, and structural dynamics modeling for the X-56A.

Figure 2 depicts exaggerated views of the first 4 longitudinal vibration modes that were significant in the system identification analysis. As the main dynamics of interest for the X-56A included the rigid-body short period (not shown), first symmetric wing bending, and first symmetric wing torsion modes, most of the present discussion is on the longitudinal dynamics. The mode numbering (i.e., 7, 9, 10, and 14) corresponds to the FEM, where the first 6 modes are associated with rigid-body degrees of freedom. Mode 7 is the first symmetric wing bending (SW1B) mode, where the wings and nose symmetrically bend up while the aft section of the center body bends down. Mode 9 is the first symmetric wing torsion (SW1T) mode, where the wings bend and twist without much fuselage motion. Mode 10 is the symmetric wing fore-aft (SFA) mode, where the wings vibrate longitudinally. Mode 14 is the symmetric winglet lateral (SWL) mode, where the winglets bend outward with bending and twisting of the wings.

The model for structural deformation of the aircraft is based on linear superposition. Assuming small deformations, the translational displacement of an arbitrary point on the aircraft about the undeformed shape is expanded as a linear combination of the structural modes as [4]

$$\mathbf{d}^P(t) = \sum_{l=1}^{n} \boldsymbol{\phi}_l^P \, \eta_l(t) \tag{1}$$

where η_l is the generalized displacement of the l^{th} structural mode. In theory, Eq. (1) involves an infinite number of modes; however, the summation is truncated after n modes for practical reasons. Each vibration mode is modeled as the second-order system

$$\ddot{\eta}_i(t) + 2\zeta_i\omega_i\dot{\eta}_i(t) + \omega_i^2\Delta\eta_i(t) = Q_i(t)/m_i \tag{2}$$

where Q_i is the generalized force acting on the mode. Later in Section VI.A, Q_i is modeled using nondimensional stability and control derivatives, similar to the aerodynamic force and moment coefficients.

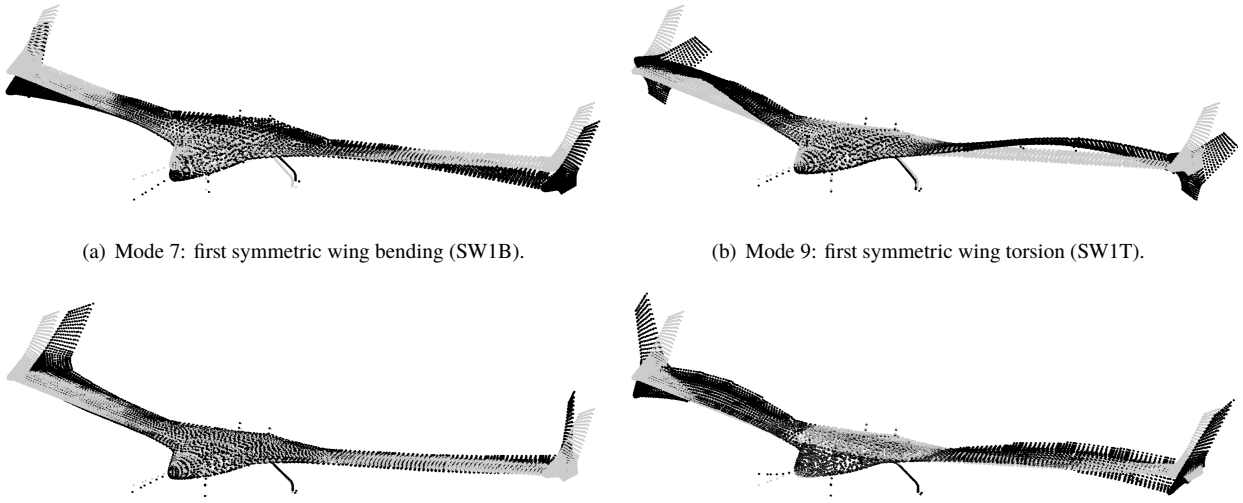

(a) Mode 7: first symmetric wing bending (SW1B).

(b) Mode 9: first symmetric wing torsion (SW1T).

(c) Mode 10: symmetric fore-aft (SFA).

(d) Mode 14: symmetric winglet lateral (SWL).

Fig. 2 Forward view of (exaggerated) longitudinal structural mode shapes (FEM configuration 24611, version 10.424_dev, $0.50w_{ff}$). Gray markers are the undeformed grid points and black markers are the deformed points.

The system identification problem for flexible aircraft is significantly more complicated than for rigid aircraft by the influence of the structural dynamics because each structural mode considered involves two states and possibly many unknown stability and control derivatives to estimate. Consequently, more data information and computation time are needed for accurate parameter estimation. The scheduling of reference condition flight variables also becomes more cumbersome because even though the aerodynamic interactions are nondimensionalized, the in-vacuo structural characteristics vary during the flight with fuel weight.

For most of the system identification analysis, structural terms (i.e., modal frequencies, damping ratios, and mode shapes) were set to known values from the FEM and GVT, based on average fuel weight over a maneuver. This choice simplified the models to linear time-invariant (LTI) systems and enabled the use of efficient frequency-domain techniques for parameter estimation, as discussed in Sections VI and VIII. This approximation necessitated short duration maneuvers for which the system properties could be assumed constant, which was accomplished using efficient excitations discussed in Section V. Any errors in the assumed structural terms were subsumed into the parameter estimates, but the structural dynamics model was judged to be sufficiently accurate for control design by comparison of the FEM model and the experimental test data. Similar to Refs. [17, 18], an attempt was made to estimate structural terms directly along with the stability and control derivatives, instead of substituting values from the FEM and GVT, but this confounded some structural and aerodynamic terms and often led to biased parameter estimates or larger uncertainties [6]. Having an accurate FEM/GVT simplified the identification problem and resulted in more accurate and more insightful parameter estimation results.

IV. Instrumentation

High-quality onboard instrumentation is critical for an accurate system identification analysis, especially for flexible aircraft with higher-order models spanning a wider frequency bandwidth. The data quality affects the signal-to-noise ratios, identifiability of the model, and the amount of useful information available for identification. Similar to the dynamic models themselves, the instrumentation for a flexible aircraft is significantly more complicated, involving many more sensors, higher sampling rates, and perhaps additional filtering than typically used for conventional rigid-body models. For this reason, an effort was made to improve the instrumentation of the X-56A over other subscale aircraft, and to increase the estimation accuracy by including dynamic models for parts of the instrumentation during the analysis.

A planform drawing with approximate location of pertinent sensors is shown in Fig. 3. Sensors not shown include the discrete strain gauges, which are concentrated along the wing and center body interfaces, and the fiber optic strain

sensor (FOSS) lines, which run along the wing span. The control surfaces are designated δ_{bfl} and δ_{bfr} for the left and right body flaps, and δ_{wfjl} and δ_{wfjr} for the left and right wing flaps, for $j = 1$ to $j = 4$ and increasing in enumeration from the wing root to the wing tip. For the longitudinal maneuvers discussed in this paper, symmetries were exploited to improve data quality and reduce modeling complexity. For example, symmetric outboard wing flap deflections were defined as

$$\delta_{wf4s} = \frac{1}{2}\left(\delta_{wf4r} + \delta_{wf4l}\right) \tag{3}$$

and designated with a subscript s to mean symmetric. Combining the data in this way reduced the effective number of control surface deflections from 10 to 5 for analyses of longitudinal motions. A similar convention was used for the symmetric accelerometer and strain gauge data.

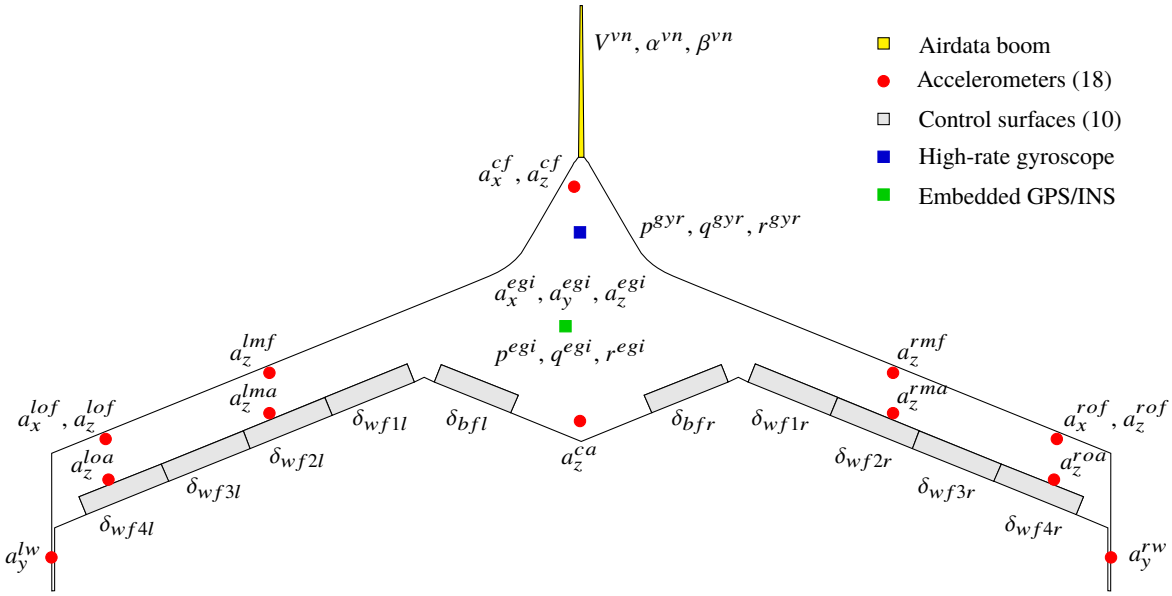

Fig. 3 X-56A planform with selected sensor and control surface locations.

Data were sampled at one of three different rates due to practical limitations of onboard computational resources. The high sampling rate was denoted f_s Hz and was reserved for channels pertinent to the faster aeroelastic dynamics. For modeling, the bandwidth of interest extended through the resonant frequency of the SW1T mode, which was at approximately $0.01 f_s$. This ratio of frequencies satisfied the general guidance that the sampling frequency should be at least 25 times the highest frequency of interest [14]. The medium sampling rate, $0.20 f_s$, was also adequate for sampling channels related to the aeroelastic dynamics. Data related to the flight condition or slowly-varying parameters, sampled at the low rate $0.02 f_s$, were either not used for modeling or were averaged over the flight condition for the analysis.

After sensors were sampled, anti-aliasing filters were applied and all data channels were resampled at $0.20 f_s$, which was about 20 times the modeling bandwidth and was adequate for identification work. Additionally, some data channels were low-pass filtered to remove noise. These filters added non-negligible phase distortions within the modeling bandwidth and were included in the analysis, which was straightforward to do using the frequency-domain techniques discussed in Section VIII, but increased the complexity of the model.

For the control surfaces indicated in Fig. 3, the digital position commands were recorded at the medium rate, whereas deflections measured with string potentiometers attached to the rotational axes of the surfaces were recorded at the high rate. A priority was placed on the control surface measurements because the frequency content of the excitations spanned the modeling bandwidth and because it was learned during the Phase 0 tests that using commands and actuator models in lieu of control surface deflection measurements would not result in the desired level of accuracy for the parameter estimates [6]. For example, Fig. 4 shows a symmetric doublet targeting the SW1B mode added to the command path for δ_{wf4s}. The left surface model prediction matched the measurement well, but the right surface had considerable error, the cause of which was not known. In other cases, it was sometimes noticed that the structural vibrations of the wing would induce uncommanded oscillations in control surface deflections, particularly when the excitation maneuvers were

started or stopped. Ground-based testing of the string potentiometers and comparison with the internal servo feedback position indicated that the sensors had no appreciable dynamics up to $0.05 f_s$, which was beyond the $0.01 f_s$ modeling bandwidth. Sixth-order analog Butterworth filters applied to each potentiometer measurement were included in the identification analysis.

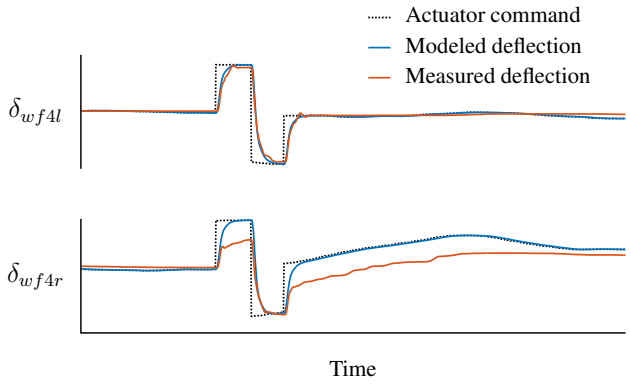

Fig. 4 Control surface data (Flight 14, FTA 6232, $0.56V_f$, $0.78w_{ff}$).

The X-56A was instrumented with 18 accelerometers, shown as red dots in Fig. 3. The embedded GPS/INS (EGI), shown in green, contained three-axis accelerometers and were sampled at the medium rate. Although this was still fast enough to observe the structural modes of interest, the sensor was located near the nominal center of mass, which was a node point for many of the structural modes, so that it mostly contributed information about the rigid-body motion of the vehicle. This was helpful to have mostly rigid-body information without higher-frequency structural contributions. The remaining accelerometers on the center body and wings were sampled at the high rate to give good resolution on the aeroelastic dynamics. These sensors were installed in pairs along the center body center line, the wing midspan, and the wing tip locations, as well as on the winglets. A second-order sensor model was included in the identification analysis for the accelerometers. Each sensor observed different amounts of each structural mode, as quantified by $\boldsymbol{\phi}$ and depicted in Fig. 2. Bode plots in Fig. 5 show empirical frequency responses from δ_{wf4s} to some symmetric accelerometer data, computed using methods described in Ref. [11] and flight test data. Locations of relevant aeroelastic frequencies, identified from the data, are also noted in these figures. The center body accelerometers were most useful for the SP and SW1B modes, although some of the SW1T mode was observable with those sensors. The midspan accelerometers did not observe much of the SW1B mode, and all accelerometers except a_z^{soa} were sensitive to the SW1T mode. The outboard x and z accelerometers were able to detect a small amount of the SFA mode. Most accelerometers could also observe the SWL mode, which had a resonant frequency just outside the excitation bandwidth.

The EGI also housed a low-bandwidth, three-axis gyroscope that was sampled at the low rate and was not usable for modeling. A high-bandwidth three-axis gyroscope was installed near the aircraft nose, as shown in blue in Fig. 3, and was sampled at the high rate. A second-order sensor model was included in the analysis for this gyroscope. This sensor observed the SP and SW1B modes well, and some SW1T response, similar to a_z^{egi} or a_z^{ca} in Fig. 5(a). Although effects from angular accelerations are registered by the accelerometers, the gyroscopes are the primary sensors for observing the rotational motion of the aircraft. It would have been helpful to have additional gyroscopes installed in the center body and the wings to attenuate errors from measurement noise and any errors in the assumed mode shapes from the FEM.

The aircraft was also instrumented with strain sensors. A total of 24 strain gauges (bending bridges and 3-gage rectangular rosettes) were installed on the center body and near the wing root, mainly for monitoring bending loads at the interface between the wings and center body during flight. Ideally, these sensors measure linear combinations of the structural displacements. Figure 6 shows Bode plots of frequency responses from δ_{wf4s} to these two types of strain gauges. Strain measurements had high signal-to-noise ratios and resulted in frequency responses of good quality. The SFA mode can be seen in the torsion strain data. In addition to the discrete strain gauges, the FOSS sensor provided a large amount of useful data, although these measurements have not yet been included in the parameter estimation.

Remaining measurements useful for system identification included airspeed, angle of attack, and sideslip angle from sensors mounted on an airdata boom ahead of the center body, and Euler angles from the EGI. These data were measured at the medium rate and were primarily useful for observing the rigid-body dynamics and the SW1B mode.

The aircraft center of mass, total mass, and inertia tensor were interpolated from tables using pre-flight and post-flight weight measurements and integrated fuel flow measurements. These data were sampled at the low rate and were then

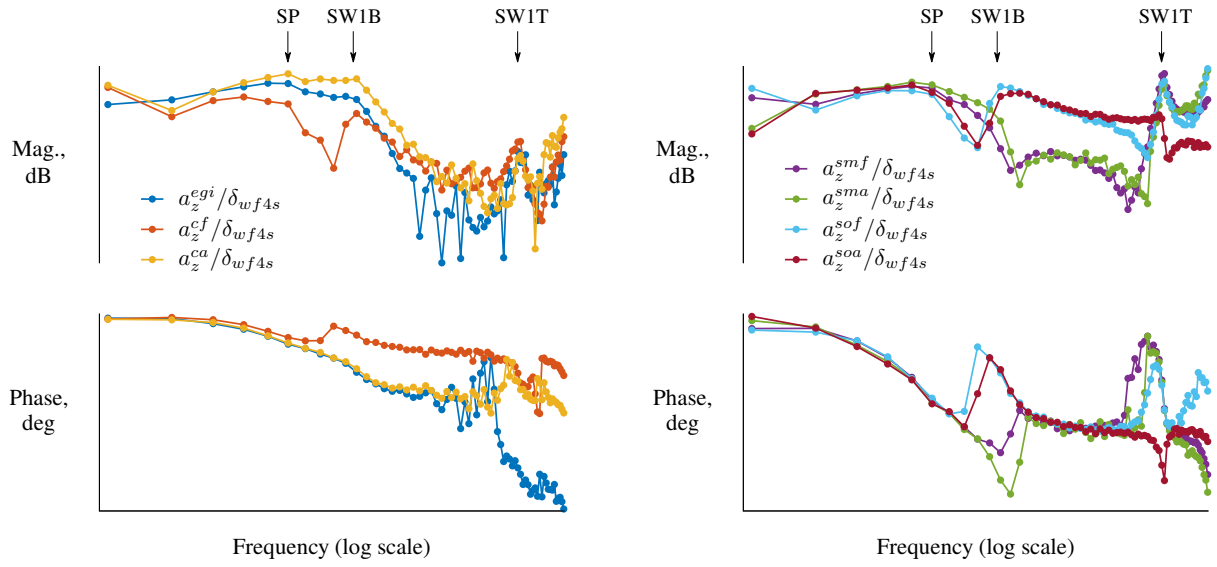

(a) Center body accelerometers.

(b) Wing accelerometers.

Fig. 5 Accelerometer frequency response data (Flight 18, FTA 506, 0.80V_f, 0.39w_{ff}).

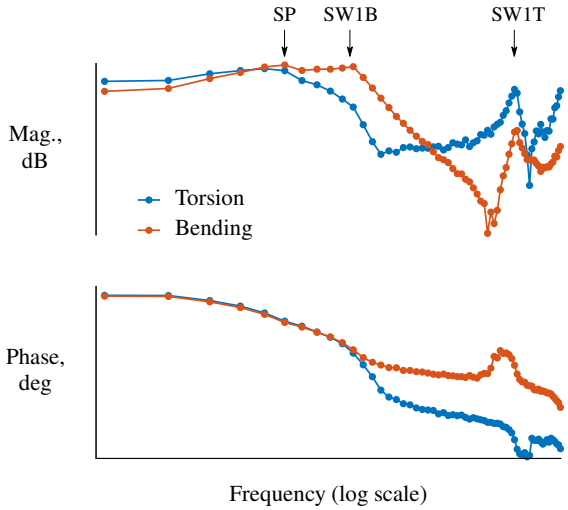

Fig. 6 Strain gauge frequency response data (Flight 18, FTA 506, 0.80V_f, 0.39w_{ff}).

averaged and held constant over a given maneuver to enable identification of LTI models. The inertias tables were populated by swinging the aircraft. Thrust levels were interpolated from ground test-based tables using measurements of engine rotation speed and total temperature of the ambient atmosphere.

When instrumenting flexible aircraft for aeroelastic modeling, many additional sensors should be used, beyond what is already required for modeling rigid-body dynamics, and these sensors should be installed in areas sensitive to the structural vibrations. Linear accelerometers should be placed where translational displacements of the structure are large, and strain sensors and gyroscopes should be installed where angular distortions are large. For example, sensors placed near the wing tips have the highest observability of the SW1B mode because the translational and rotational displacements are the largest there, as shown in Fig. 2(a). Multiple spanwise locations provide information on different bending modes, whereas multiple chordwise locations provide information on different torsion modes.

Having a symmetry between the left and right sides of the aircraft allows for the signals to decouple into symmetric and anti-symmetric motions, which can help simplify the analysis into decoupled longitudinal and lateral-directional models. The main structural modes for the X-56A involved the wings moving in the body z-axis, which is one reason why most accelerometers measured vertical components. However the x-axis and y-axis accelerometers were important for observing the SFA and SWL modes.

V. Experiment Design

A. Overview

The maneuvers for system identification were small-perturbation excitations about reference flight conditions at low angles of attack. There were several challenges and constraints for the experiment design. Most importantly, maneuvers had to be short in duration because the aircraft consumes fuel quickly, which changes the dynamics, and because there were many test points and experiments to complete in each flight. Maneuvers also had to generate responses that were small enough in amplitude for linear modeling over the bandwidth of interest, but that were large enough to achieve good signal-to-noise ratios, while remaining within operational and load limits. The inputs needed to be robust to changes in the dynamics (e.g., modal frequencies) with fuel weight, airspeed, altitude, and control law. Lastly, a large number of control effectors were to be modeled.

Maneuvers for the identification of stability and control derivatives were designed using orthogonal phase-optimized multisines [14], which are of the form

$$\mu_j(t) = \sum_{k \in K_j} a_k \sin\left(\frac{2\pi k}{T} t + \phi_k\right) \tag{4}$$

The inputs are summations of sinusoids, which have harmonic frequencies k/T for a given excitation time duration T. The power spectra a_k can be chosen arbitrarily, and the phase angles ϕ_k are optimized for minimum relative peak factor (RPF). When there are multiple inputs, the harmonics are distributed amongst the inputs and are collected into the sets K_j for $j = 1, 2, \ldots, n_u$.

As shown in Fig. 7, the multisines were added to the command path at the actuators, after the control law and mixer. Selecting this location within the flight control architecture was important for accurate identification of stability and control derivatives of the bare-airframe dynamics from closed-loop data [11, 14], as discussed more in Section VIII.

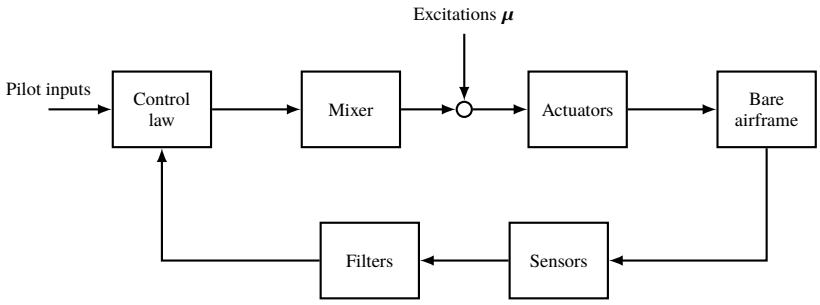

Fig. 7 Block diagram of the flight control and excitation inputs.

Using these multisines for the experiment design had several advantages. First, the multisines are mutually orthogonal and were applied to the respective inputs simultaneously, rather than sequentially, which significantly reduced the maneuver duration and resulted in only small changes in the fuel weight and flight condition. Second, the multisines produced small-perturbation data about the reference condition, which was good for linear modeling. Also, explicitly designing the excitation bandwidth and power spectra tailored the experiment and the analysis around the modes of interest. Lastly, the multisines produced data conducive for a variety of parameter estimation techniques, as elaborated in Section VIII.

B. Multisine Designs

Table 1 summarizes the multisines designed for extracting stability and control derivatives from the Phase 1 flight tests. The first column shows the flight test aid (FTA) designation, which was the unique number assigned to each set of multisines. The multisines were grouped into three categories, which were separated in the table by the horizontal lines: FTA 500–526 have symmetric excitation of the control effectors, FTA 530–547 have antisymmetric excitation, and FTA 550–576 have independent excitation. This partitioning allowed for the identification of decoupled longitudinal and lateral-directional models, which significantly reduced the modeling complexity. Each multisine design was scaled to three different amplitudes (low, medium, and high) to achieve adequate response sizes over the entire flight envelope. For example, FTA 506–508 are the same waveforms, but the larger-amplitude FTA 508 was intended for lower airspeeds whereas the smaller-amplitude FTA 506 was intended for higher airspeeds. Multisine amplitudes were scaled using linear and nonlinear closed-loop simulations, and verified through flight testing.

Table 1 Multisine designs for the X-56A Phase 1 flights.

		Number of inputs		Frequencies per input		Targeted modes					
FTA	Duration	Surf.	Thr.	Surf.	Thr.	PH	DR	SP	RS	LE	HE
500–502	T	5	0	12	0			X			
503–505	T	5	0	25	0			X		X	
506–508	T	5	0	65	0			X		X	X
509–511	$4T$	5	0	25	0	X		X			
512–514	$4T$	5	0	51	0	X		X		X	
515–517	$4T$	5	0	66	0	X		X		X	X
518–520	$4T$	5	1	24	4	X		X			
521–523	$4T$	5	1	50	4	X		X		X	
524–526	$4T$	5	1	66	2	X		X		X	X
530–532	T	5	0	13	0		X		X		
533–535	T	5	0	25	0		X		X	X	
536–538	T	5	0	65	0		X		X	X	X
539–541	$4T$	5	1	10	2		X		X		
542–544	$4T$	5	1	22	2		X		X	X	
545–547	$4T$	5	1	64	2		X		X	X	X
550–552	T	10	0	7	0		X	X	X		
553–555	T	10	0	13	0		X	X	X	X	
556–558	T	10	0	33	0		X	X	X	X	X
559–561	$4T$	10	0	13	0	X	X	X	X		
562–564	$4T$	10	0	25	0	X	X	X	X	X	
565–567	$4T$	10	0	66	0	X	X	X	X	X	X
568–570	$4T$	10	2	13	2	X	X	X	X		
571–573	$4T$	10	2	25	2	X	X	X	X	X	
574–576	$4T$	10	2	66	2	X	X	X	X	X	X

Because the excitation frequencies are harmonics of a fundamental frequency, the excitation time duration, number of inputs excited, and frequency resolution of the inputs are interrelated. To achieve a good balance over many designs, two time durations, T and $4T$ were selected. The duration T was relatively short, even in comparison to inputs designed for rigid body modeling, but provided good frequency resolution on the aeroelastic modes of interest for 5 inputs while keeping fuel weight changes under 1%. The duration $4T$ resulted in fuel weight changes up to 3%, but allowed for a finer resolution in frequency and more control effectors to be moved at the same time. The FTAs with throttle excitations included only a few harmonics because of software limitations but were successful in exciting phugoid motions.

The main differences between the multisines are the modes targeted by the excitations. The rigid body modes are denoted PH for phugoid, DR for dutch roll, SP for short period, and RS for roll subsidence. The other names LE and HE stand for low elastic (structural modes 7–8) and high elastic (structural modes 9–14), which are relative names. Although the frequencies of the modes varied with the flight condition, the multisines were designed with uniform spectra that spanned those ranges, so that the modes of interest were always excited using a relatively small number of FTAs.

The phase angles for the multisine designs were optimized using a simplex method. Due to the extended bandwidth and frequency resolution needed for aeroelastic identification, there were many more phase angles than in typical designs for rigid-body identification. The SIDPAC routine `mkmsswp.m` was modified to run using the MATLAB® Parallel Computing Toolbox™ and processed all 24 sets of multisines overnight on a standard laptop computer. An alternative approach, which was used in Ref. [19], is to randomly generate phase angles until sufficiently low RPF values were obtained. For the X-56A designs, this approach avoided the time-consuming optimization but still needed many trials to attain comparable designs.

C. "High Elastic Lon" design, FTA 506–508

The multisines FTA 506–508 were the primary excitations used for identification during the Phase 1 flights. These inputs included symmetric movement of the 5 control surface pairs at 65 frequencies over time duration T. The excitation bandwidth included the SP, SW1B, SW1T, and SFA modes. The excitation bandwidth ended just below the SWL resonant frequency; however, some response from that mode was usually still present. To prevent subsequent frequencies on adjacent surfaces, the harmonics were distributed in the following order: δ_{bfs}, δ_{wf3s}, δ_{wf1s}, δ_{wf4s}, δ_{wf2s}. Relative scalings of 1.00, 0.95, 0.90, 0.85 and 0.80 were applied to the excitations from δ_{bfs} to δ_{wf4s} to help balance the response amplitudes, i.e., so that the pitching motion created by the larger moment arm from δ_{wf4s} did not overwhelm the response by δ_{bfs}. As mentioned in Section VIII.D, the amplitudes for δ_{bfs} and δ_{wf1s} should have been further increased relative to the other surfaces to achieve higher signal-to-noise ratios. It was suspected that propulsion interaction effects or the thicker fuselage at those stations resulted in a control effectiveness being lower than expected.

Figure 8 shows control surface deflection measurements from flight test data for one complete period of the input. The flight test condition was at 109% of the flutter speed, which resulted in considerable control activity, particularly for δ_{wf1s}. The surface deflection measurements contained a large amount of deterministic content over a wide bandwidth and only a small amount of measurement noise.

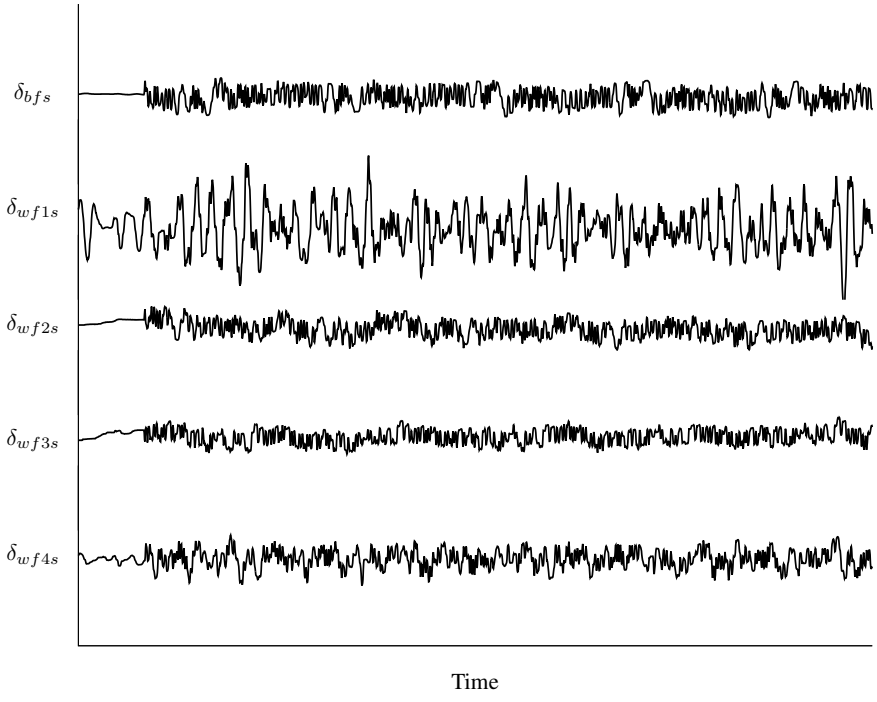

Fig. 8 Control surface deflections (Flight 39, FTA 507, $1.09V_f$, $0.71w_{ff}$).

The designed perturbations were orthogonal and therefore had pairwise correlations equal to zero. The actual control surface deflections had higher pairwise correlations due to the additional feedback and mixing. Figure 9(a) is a plot matrix of the flight data from Fig. 8. The diagonals list the names of the five control surfaces. The upper triangle shows cross plots of the data. These plots appear scattered and are not straight lines, which visually confirms the low data correlations. The lower triangle indicates the pairwise correlation coefficients between the input pairs. The largest correlation was 0.40 and the remaining values were below 0.16. It is recommended for identification using equation error and output error that the correlations remain below about 0.9 in absolute value [14], which was the case here, even with the feedback control law actively suppressing the open-loop flutter instability. For more stable flight at lower airspeeds, input correlations were generally much lower in absolute value due to less feedback activity.

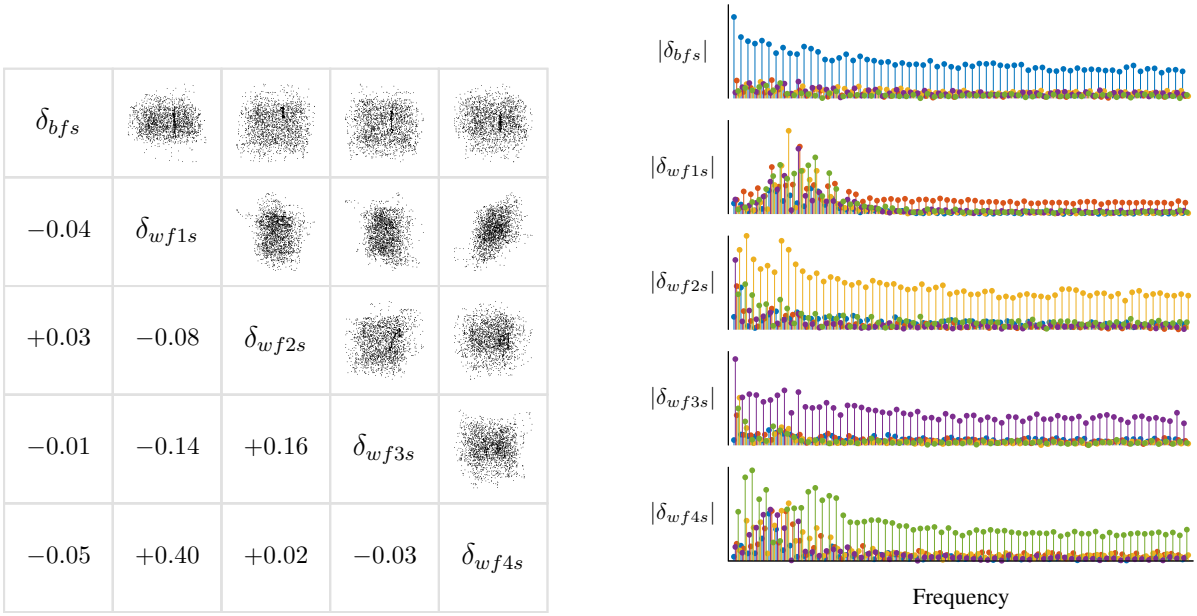

(a) Correlation cross plots.

(b) Fourier transforms.

Fig. 9 Control surface content (Flight 39, FTA 507, 1.09V_f, 0.71w_{ff}).

Frequency spectra are shown in Fig. 9(b) as absolute values of Fourier transform data at the harmonic frequencies. Different y-axis scales are for each plot used to better show the content, and different colors are used to differentiate between the excitation designs. The multisines were designed to be orthogonal and with uniform spectra, but the amplitudes decreased with frequency due to the actuator dynamics, and there were distortions of the uniform spectra due to the control law. However, these factors were not important for the parameter estimation. Note that all frequencies are present on all channels due to the feedback and mixing, although the primary multisine frequencies are the largest. The SP and SW1B modes are most evident in the feedback on δ_{wf1s} and δ_{wf4s}.

The FTA 506–508 multisines were highly effective in facilitating accurate modeling of the aeroelastic flight dynamics. These multisines successfully excited the modes of interest over the entire flight envelope using 5 inputs in decorrelated ways. Maneuvers were relatively short in duration and enabled the use of efficient frequency-domain techniques for identifying LTI models. Furthermore, these maneuvers were designed before the Phase 1 flight tests with little prior information about the aircraft dynamics beyond approximate modal frequencies and response amplitudes.

D. "Mini GVT" design, FTA 503–505

The multisines FTA 503–505 were similar to FTA 506–508, but only included the first elastic mode and had fewer harmonics per input. In addition to providing excitation during flight, another use of the multisine was to conduct an ad hoc GVT test on the runway before and after each flight. From these tests, accelerometer and strain data were helpful in quickly determining if any significant damage had occurred to the aircraft during flight.

A typical example is shown in Fig. 10 for Flight 37, during which the flutter speed was surpassed. The data are

Fourier transform magnitudes for a symmetric pair of bending strain gauges. The largest peak was roughly the same before and after the flight, with only a small change in frequency and amplitude due to burning 89% of the fuel during flight. The resonant peak corresponded to the SW1B mode and is significantly lower than observed in flight because the aircraft was on the runway and had different boundary conditions. The smaller secondary peak in the pre-flight data is another structural mode, but was typically attenuated in the post-flight data that had lower fuel weight.

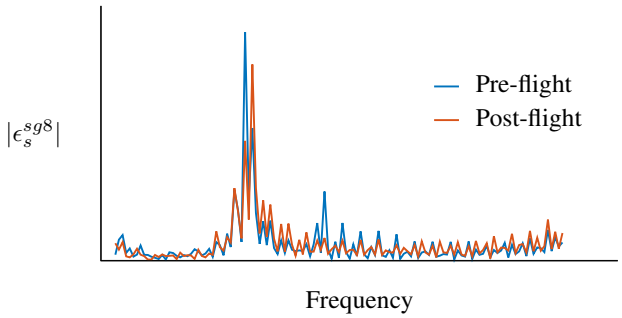

Fig. 10 Strain gauge Fourier transforms for mini-GVT maneuvers (Flight 37, FTA 503).

VI. Flight Dynamics Model Postulation

A. Equations of Motion

The aeroelastic flight dynamics model follows the mean-axis formulation derived in Ref. [20] and further developed in Refs. [4, 21]. For small perturbations about reference flight conditions, the model can be specified as the state-space equations

$$\dot{\mathbf{x}}(t) = \mathbf{A}\,\mathbf{x}(t) + \mathbf{B}\,\mathbf{u}(t) \tag{5a}$$

$$\mathbf{y}(t) = \mathbf{C}\,\mathbf{x}(t) + \mathbf{D}\,\mathbf{u}(t) \tag{5b}$$

or the transfer function matrix

$$\mathbf{H}(s) = \frac{\mathbf{y}(s)}{\mathbf{u}(s)} = \mathbf{C}\,(s\mathbb{I} - \mathbf{A})^{-1}\,\mathbf{B} + \mathbf{D} \tag{6}$$

where the system matrices **A**, **B**, **C**, and **D** are constants that depend on the flight condition.

The inputs for most of the identified longitudinal models were the symmetric control surface deflections

$$\mathbf{u} = \begin{bmatrix} \Delta\delta_{bfs} & \Delta\delta_{wf1s} & \Delta\delta_{wf2s} & \Delta\delta_{wf3s} & \Delta\delta_{wf4s} \end{bmatrix}^T \tag{7}$$

The model states were partitioned into rigid-body states for the short period mode

$$\mathbf{x}_r = \begin{bmatrix} \Delta\alpha & q & \Delta\theta \end{bmatrix}^T \tag{8}$$

and elastic states for the included structural modes

$$\mathbf{x}_e = \begin{bmatrix} \Delta\eta_1 & \dots & \Delta\eta_n & \dot{\eta}_1 & \dots & \dot{\eta}_n \end{bmatrix}^T \tag{9}$$

Using the in-vacuo structural displacements and rates as states, as opposed to other possible choices, considerably reduces the model complexity [4]. Together, the state vector for analysis was

$$\mathbf{x} = \begin{bmatrix} \mathbf{x}_r \\ \mathbf{x}_e \end{bmatrix} \tag{10}$$

The aerodynamic forces and moments and the generalized forces acting on the longitudinal degrees of freedom are expanded as linear Taylor series using the states and controls as

$$Z = Z_\alpha \Delta\alpha + Z_q q + \sum_{l=1}^{n} Z_{\eta_l} \Delta\eta_l + \sum_{l=1}^{n} Z_{\dot{\eta}_l} \dot{\eta}_l + \sum_{j=1}^{n_u} Z_{\delta_j} \Delta\delta_j \tag{11a}$$

$$M = M_\alpha \Delta\alpha + M_q q + \sum_{l=1}^{n} M_{\eta_l} \Delta\eta_l + \sum_{l=1}^{n} M_{\dot{\eta}_l} \dot{\eta}_l + \sum_{j=1}^{n_u} M_{\delta_j} \Delta\delta_j \tag{11b}$$

$$Q_i = Q_{i_\alpha} \Delta\alpha + Q_{i_q} q + \sum_{l=1}^{n} Q_{i_{\eta_l}} \Delta\eta_l + \sum_{l=1}^{n} Q_{i_{\dot{\eta}_l}} \dot{\eta}_l + \sum_{j=1}^{n_u} Q_{i_{\delta_j}} \Delta\delta_j \tag{11c}$$

for $i = 1, 2, \ldots, n$. The derivatives in Eq. (11) are defined in terms of the nondimensional counterparts as

$$Z_\alpha = \frac{\bar{q}S}{mV} C_{Z_\alpha} \qquad Z_q = \frac{\bar{q}S}{mV}\frac{\bar{c}}{2V} C_{Z_q} \qquad Z_{\eta_l} = \frac{\bar{q}S}{mV} C_{Z_{\eta_l}} \qquad Z_{\dot{\eta}_l} = \frac{\bar{q}S}{mV}\frac{\bar{c}}{2V} C_{Z_{\dot{\eta}_l}} \qquad Z_{\delta_j} = \frac{\bar{q}S}{mV} C_{Z_{\delta_j}} \tag{12a}$$

$$M_\alpha = \frac{\bar{q}S\bar{c}}{I_{yy}} C_{m_\alpha} \qquad M_q = \frac{\bar{q}S\bar{c}}{I_{yy}}\frac{\bar{c}}{2V} C_{m_q} \qquad M_{\eta_l} = \frac{\bar{q}S\bar{c}}{I_{yy}} C_{m_{\eta_l}} \qquad M_{\dot{\eta}_l} = \frac{\bar{q}S\bar{c}}{I_{yy}}\frac{\bar{c}}{2V} C_{m_{\dot{\eta}_l}} \qquad M_{\delta_j} = \frac{\bar{q}S\bar{c}}{I_{yy}} C_{m_{\delta_j}} \tag{12b}$$

$$Q_{i_\alpha} = \frac{\bar{q}S\bar{c}}{m_i} C_{Q_{i_\alpha}} \qquad Q_{i_q} = \frac{\bar{q}S\bar{c}}{m_i}\frac{\bar{c}}{2V} C_{Q_{i_q}} \qquad Q_{i_{\eta_l}} = \frac{\bar{q}S\bar{c}}{m_i} C_{Q_{i_{\eta_l}}} \qquad Q_{i_{\dot{\eta}_l}} = \frac{\bar{q}S\bar{c}}{m_i}\frac{\bar{c}}{2V} C_{Q_{i_{\dot{\eta}_l}}} \qquad Q_{i_{\delta_j}} = \frac{\bar{q}S\bar{c}}{m_i} C_{Q_{i_{\delta_j}}} \tag{12c}$$

These nondimensional stability and control derivatives were the model parameters estimated from the data, which allowed for direct comparison over different flight conditions and with wind tunnel or simulation models.

Similar to the state vector, the state-space equations of motion in Eq. (5a) can be partitioned based on the rigid and elastic terms as

$$\begin{bmatrix} \dot{\mathbf{x}}_r \\ \dot{\mathbf{x}}_e \end{bmatrix} = \begin{bmatrix} \mathbf{A}_{rr} & \mathbf{A}_{re} \\ \mathbf{A}_{er} & \mathbf{A}_{ee} \end{bmatrix} \begin{bmatrix} \mathbf{x}_r \\ \mathbf{x}_e \end{bmatrix} + \begin{bmatrix} \mathbf{B}_r \\ \mathbf{B}_e \end{bmatrix} \mathbf{u} \tag{13}$$

The $\mathbf{A}_{rr}$ and $\mathbf{B}_r$ matrices quantify how the rigid states and controls drive the rigid-body motion, and are the traditional equations for flight dynamics, e.g., as discussed in Ref. [5]. Considering the short period approximation,

$$\mathbf{A}_{rr} = \begin{bmatrix} Z_\alpha & Z_q & 0 \\ M_\alpha & M_q & 0 \\ 0 & 0 & 0 \end{bmatrix} + \begin{bmatrix} \frac{-X_T \cos\alpha}{mV} + \frac{g\sin\gamma}{V} & 1 & -\frac{g\sin\gamma}{V} \\ 0 & 0 & 0 \\ 0 & 1 & 0 \end{bmatrix} \tag{14a}$$

$$\mathbf{B}_r = \begin{bmatrix} Z_{\delta_{bfs}} & Z_{\delta_{wf1s}} & Z_{\delta_{wf2s}} & Z_{\delta_{wf3s}} & Z_{\delta_{wf4s}} \\ M_{\delta_{bfs}} & M_{\delta_{wf1s}} & M_{\delta_{wf2s}} & M_{\delta_{wf3s}} & M_{\delta_{wf4s}} \\ 0 & 0 & 0 & 0 & 0 \end{bmatrix} \tag{14b}$$

where $\mathbf{A}_{rr}$ has been decomposed into two matrices to show the contributions from the aerodynamics and from other sources. Likewise, the $\mathbf{A}_{ee}$ and $\mathbf{B}_e$ matrices quantify how the elastic states and controls drive the elastic motion, and are

$$\mathbf{A}_{ee} = \begin{bmatrix} 0 & \cdots & 0 & 0 & \cdots & 0 \\ \vdots & \ddots & \vdots & \vdots & \ddots & \vdots \\ 0 & \cdots & 0 & 0 & \cdots & 0 \\ Q_{1_{\eta_1}} & \cdots & Q_{1_{\eta_n}} & Q_{1_{\dot{\eta}_1}} & \cdots & Q_{1_{\dot{\eta}_n}} \\ \vdots & \ddots & \vdots & \vdots & \ddots & \vdots \\ Q_{n_{\eta_{\eta_1}}} & \cdots & Q_{n_{\eta_{\eta_n}\eta_n}} & Q_{n_{\eta_{\dot{\eta}_1}}} & \cdots & Q_{n_{\eta_{\dot{\eta}_n}\eta_n}} \end{bmatrix} + \begin{bmatrix} 0 & \cdots & 0 & 1 & \cdots & 0 \\ \vdots & \ddots & \vdots & \vdots & \ddots & \vdots \\ 0 & \cdots & 0 & 0 & \cdots & 1 \\ -\omega_1^2 & \cdots & 0 & -2\zeta_1\omega_1 & \cdots & 0 \\ \vdots & \ddots & \vdots & \vdots & \ddots & \vdots \\ 0 & \cdots & -\omega_{n_\eta}^2 & 0 & \cdots & -2\zeta_{n_\eta}\omega_{n_\eta} \end{bmatrix} \tag{15a}$$

$$\mathbf{B}_e = \begin{bmatrix} 0 & 0 & 0 & 0 & 0 \\ \vdots & \vdots & \vdots & \vdots & \vdots \\ 0 & 0 & 0 & 0 & 0 \\ Q_{1_{\delta bfs}} & Q_{1_{\delta wf1s}} & Q_{1_{\delta wf2s}} & Q_{1_{\delta wf3s}} & Q_{1_{\delta wf4s}} \\ \vdots & \vdots & \vdots & \vdots & \vdots \\ Q_{n_{\delta bfs}} & Q_{n_{\delta wf1s}} & Q_{n_{\delta wf2s}} & Q_{n_{\delta wf3s}} & Q_{n_{\delta wf4s}} \end{bmatrix} \tag{15b}$$

The kinematic terms in $\mathbf{A}_{ee}$ resemble a damped harmonic oscillator and result from rearranging Eq. (2). The remaining terms in Eq. (13) are the off-diagonal submatrices, which quantify the coupling between the rigid and elastic states. These matrices are defined as

$$\mathbf{A}_{er} = \begin{bmatrix} 0 & 0 & 0 \\ \vdots & \vdots & \vdots \\ 0 & 0 & 0 \\ Q_{1_\alpha} & Q_{1_q} & 0 \\ \vdots & \vdots & \vdots \\ Q_{n_\alpha} & Q_{n_q} & 0 \end{bmatrix} \qquad \mathbf{A}_{re} = \begin{bmatrix} Z_{\eta_1} & \dots & Z_{\eta_n} & Z_{\dot{\eta}_1} & \dots & Z_{\dot{\eta}_n} \\ M_{\eta_1} & \dots & M_{\eta_n} & M_{\dot{\eta}_1} & \dots & M_{\dot{\eta}_n} \\ 0 & \dots & 0 & 0 & \dots & 0 \end{bmatrix} \tag{16a}$$

and consist of only stability derivatives and not any other sources of coupling.

References [22, 23] suggest that if the lowest structural frequency is at least 5 times the highest rigid-body frequency, there is a time-scale separation sufficient to neglect $\mathbf{A}_{re}$. In this case, the structural vibrations appear in the measurements but do not affect the rigid-body motion of the aircraft. The modal frequencies for the X-56A varied with airspeed and fuel weight, and had a maximum separation factor of 3.6 between the longitudinal rigid-body and structural modes during the Phase 1 flights. By this guideline, it was expected that the aerodynamic coupling in $\mathbf{A}_{re}$ was not negligible for the X-56A, which was confirmed by the consistent estimates determined for many of the coupling stability derivatives in that matrix.

Similar to the state equations, the output equations in Eq. (5b) can be partitioned as

$$\mathbf{y} = \begin{bmatrix} \mathbf{C}_r & \mathbf{C}_e \end{bmatrix} \begin{bmatrix} \mathbf{x}_r \\ \mathbf{x}_e \end{bmatrix} + \mathbf{D}\,\mathbf{u} \tag{17}$$

Both nonlinear and linearized expressions of the output equations for the sensors used for modeling the X-56A are derived in Ref. [8], including for accelerometers, strain gauges, gyroscopes, angle-of-attack vanes, etc.

The effects of the structural vibrations on the measured outputs, as quantified by the $\mathbf{C}_e$ matrix, were significant. The added content needed to be considered during the control design, particularly near the flutter speed. For example, Bode plots from the outboard symmetric surface deflection to the pitch rate gyroscope and the fore z-axis accelerometer on the center body, both of which were used for feedback, are shown in Fig. 11. These Bode plots were generated from linear models where stability and control derivatives were obtained using ZAERO$^{\text{TM}}$, as in Ref. [16]. The red lines show the frequency response of the full model, including all 25 modeled structural modes. The blue lines show the assumed frequency response if the structural dynamics were neglected, i.e., $\mathbf{C}_e = \mathbf{0}$. There are significant differences between the two frequency responses, particularly near the SW1B mode and within the operating bandwidth of the control law.

The aeroelastic model summarized in this section represents a practical simplification of higher-order aeroelastic modeling tools based on the traditional flight dynamics concepts of quasi-steady aerodynamics and of stability and control derivatives. This formulation, which was able to predict the flutter mechanism for the X-56A, made the system identification problem tractable. However, the model structure was still significantly more complicated than for conventional rigid-body models, which introduced a number of challenges for identification.

As the number of vibration modes increases, the number of possible stability and control derivatives to estimate (not including any unknown initial conditions, biases, or scale factors) increases quadratically. For example, a traditional short period model may consist of up to 6 parameters, whereas for the X-56A, 14 derivatives are present due to the large number of symmetric inputs. As the first and second structural modes are included, the number of derivatives increases to 27 and 44, respectively, which is very large in comparison. As the model complexity increases, so do the computational requirements for parameter estimation using iterative techniques. Consequently, more data information is

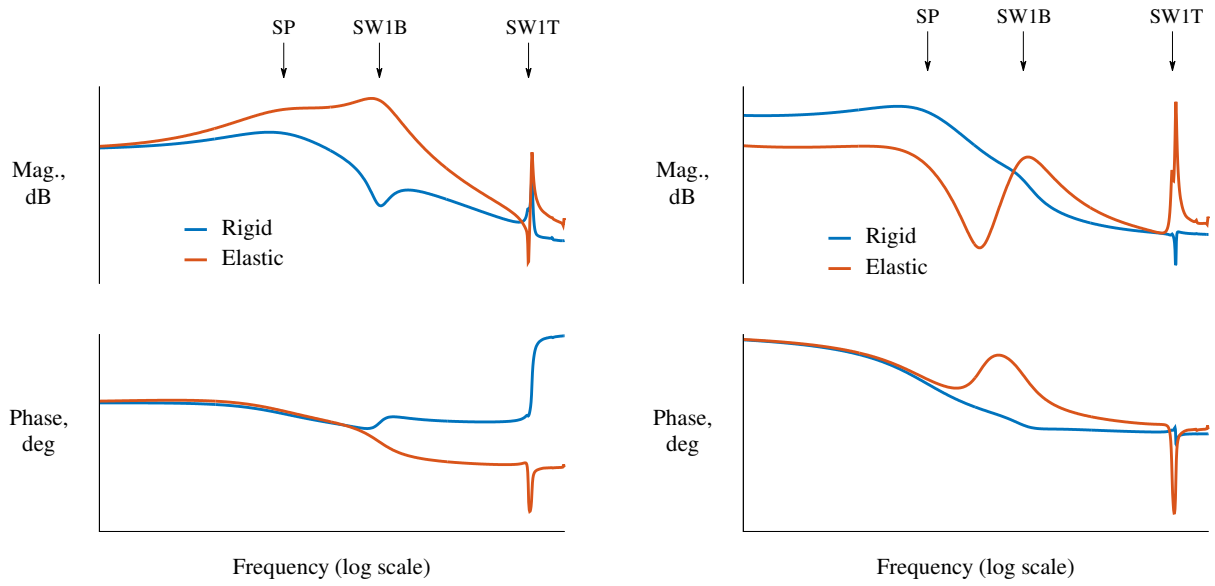

(a) q^{gyr}/δ_{wf4s}.

(b) a_z^{cf}/δ_{wf4s}.

Fig. 11 Effect of structural dynamics on measurements using a simulation model.

typically needed to provide information for the parameters, which again increases the model complexity. Some aspects of model order reduction are discussed next in Section VI.B, and choosing model parameters in Section VIII.

Another challenge involved the efficient construction of state models and bookkeeping of aeroelastic parameters during the estimation. Computational efficiency was important because some of the parameter estimation methods discussed in Section VIII are iterative and involve repeated construction of the state models. Furthermore, the model construction needed to be flexible, as different combinations of inputs, outputs, structural modes, and model parameters were adjusted. A significant simplification was assuming LTI models, so that variables for the flight condition could be averaged over a given maneuver. This assumption was supported by the short-duration maneuvers described in Section V, and facilitated efficient analyses based in the frequency domain, rather than time domain. It was helpful to pass matrices of indices to the estimator to indicate which inputs, outputs, and vibration modes to use, as well as which stability and control derivatives, time delays, and structural parameters to estimate.

B. Model Order Reduction

Figure 12 shows the frequency content of two accelerometers up to the Nyquist frequency for the medium sample rate from a flight test maneuver. There is significant content beyond the frequency bandwidth of interest for the modeling (up to the SW1T mode), which is in part due to higher-frequency structural modes excited by ambient air and the internal couplings of the flight dynamics. Rather than attempting to model all of this content, reduced-order models (ROM) were identified.

As discussed in Refs. [4, 24], a static-elastic residualization of the structural modes yields a more accurate representation of the system dynamics than does model truncation. Figure 13 shows an example of the effect of model order reduction on some pitching moment stability and control derivatives using the linear simulation model. Results were similar for the other derivatives. The red lines are the values for the full model. The blue dots show the stability and control derivatives extracted from the ROMs as the number of included structural modes is increased. Zero structural modes indicates that only the rigid-body modes were retained, and 25 structural modes denotes the full simulation model. Zero-lines are also shown in gray. A low-speed case with parameters from a maneuver in Flight 11 is shown in Fig. 13(a) and a high-speed case beyond the flutter speed with parameters from a maneuver in Flight 39 is shown in Fig. 13(b).

In the low-speed case, the derivatives had a small bias when only the rigid-body dynamics were included. Including the first structural mode (SW1B) increased this bias. Adding the second structural mode did not reduce this bias because

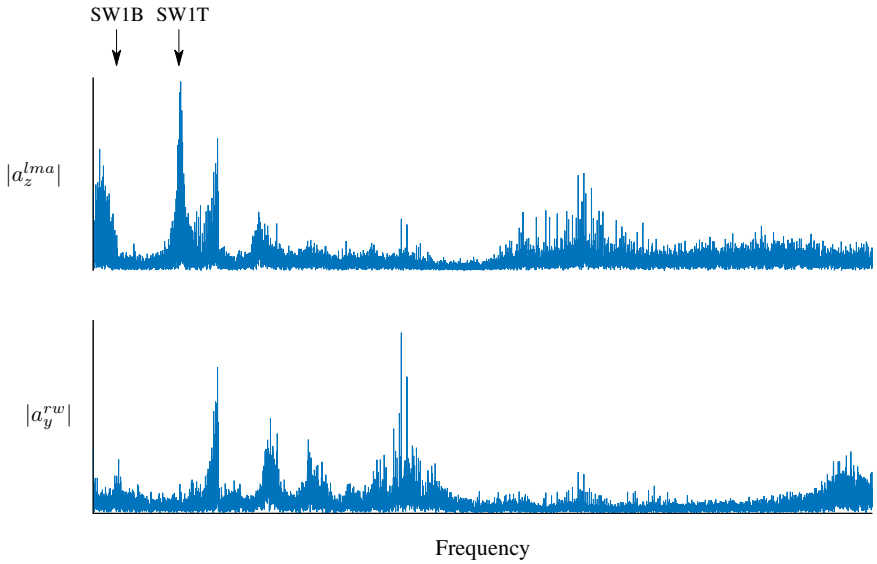

Fig. 12 Accelerometer Fourier transforms (Flight 11, FTA 506, 0.65V_f, 0.28w_{ff}).

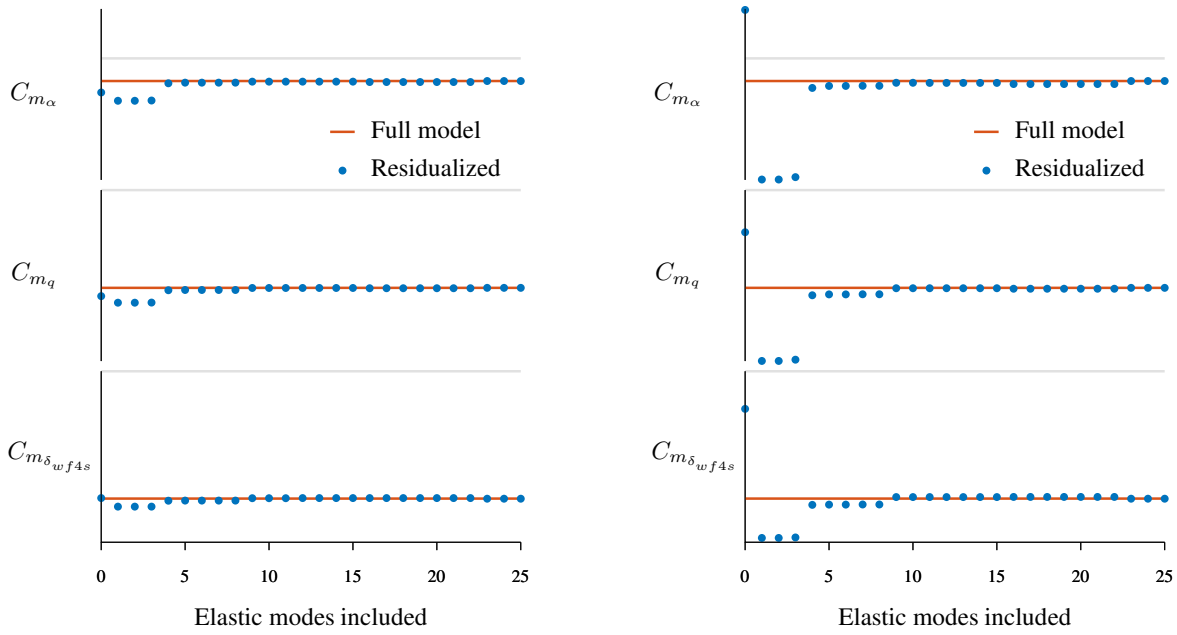

(a) Low speed (0.63V_f). (b) High speed (1.08V_f).

Fig. 13 Effect of model reduction on stability and control derivatives for the simulation model.

it is the antisymmetric first wing bending mode and does not significantly affect the longitudinal dynamics. It was surprising that adding the third structural mode, SW1T, did not significantly impact the bias either. The fourth mode, SFA, was needed to reduce the bias to within 10% of the true parameter. Therefore, the longitudinal dynamics were expected to need the short period, SW1B, SW1T, and SFA modes for accurate identification of stability and control derivatives at low speeds.

In the high-speed case, there was a larger difference between the true and residualized derivatives. Only including the rigid-body modes gave much larger errors than at low speeds, and C_{m_α} had the wrong sign. Errors were larger than in the low-speed case for a given number of structural modes, or equivalently, more structural modes were needed to

obtain the same level of accuracy. This requirement on the increased fidelity of the structural dynamics model was one reason why identification near the flutter speed from flight test data was difficult, as discussed in Section VIII.D.

VII. Data Synchronization and Kinematic Consistency

As discussed previously in Section IV, data quality is crucial for accurately identifying aeroelastic models. In addition to the aspects already mentioned, it is important that the data are synchronized in time and are free of sensor errors.

During a system identification analysis, relative time skews between different channels of measured data can manifest as phase lags in the identified system dynamics, which degrades the accuracy of estimated parameters [25]. For the input-output parameter estimation techniques discussed in Sections VIII.A and VIII.B, time delays were estimated directly during the parameter estimation, rather than correcting the data before the analysis. It was assumed that all the inputs (potentiometers on the control surfaces) had negligible delays relative to each other, and one time delay was estimated for each output. It was simpler to work with the state-space matrices in Eq. (5) directly, rather than assemble state-space objects within MATLAB®, so that the delay parameters could take arbitrary values including non-integer multiples of the sampling period and negative numbers. In the frequency domain, this was implemented by multiplying each output Fourier transform or frequency response by $e^{-j\omega\tau}$, where τ is the respective time delay.

For the equation-error analysis discussed in Section VIII.C, data were synchronized before the analysis. The accelerometers were first synchronized by comparing Fourier transforms over the rigid-body bandwidth, which should be the same [8], and estimating relative time skews using output error in the frequency domain [26]. After the accelerometers were synchronized, kinematic relations were used to similarly synchronize the angular rates and angle of attack data to the accelerometer data over the rigid-body frequencies. Similarly, Euler angles were synchronized to integrated angular rate data, and strain data were synchronized to accelerometer data over frequencies near the SW1T mode. Again, relative time skews between the control surface measurements were neglected. This approach was ad hoc in that the frequency bands for comparison needed to be selected by the analyst, but the approach improved the estimation results. For an accurate real-time analysis, all the time skews would have to be calibrated before the flight, or time skews would be subsumed into the stability and control derivatives.

Data compatibility errors, for example arising from sensor biases and scale factor corrections, can degrade the accuracy of estimated stability and control derivatives. However, these errors were not an important factor for this analysis. Because the identification analysis was performed in the frequency domain, as discussed in Section VIII, low-frequency content was discarded during the Fourier transform step, which automatically removed bias errors from the data [14]. Furthermore, the primary aeroelastic sensors used (accelerometers and gyroscopes) typically have negligible scale factor errors. Lastly, because many more sensors were involved than for typical analyses of rigid-body dynamics, redundant data provided some robustness to data compatibility errors. For the output-error analysis discussed in Section VIII.A, scale factor parameters were estimated for the air flow angle vane and gyroscope measurements, but were small and made a negligible difference in the values of the stability and control derivatives.

VIII. Modeling Approaches

A variety of modeling approaches were used to estimate stability and control derivatives due to the complicated nature of the aeroelastic vehicle dynamics. Each method provided different insights into the modeling, and confidence was gained in the results when similar solutions were obtained. All of the approaches used a maximum likelihood estimator and frequency-domain data. The methods used were output error, frequency response error, and equation error, which are explained in more detail in Ref. [14].

A. Output Error

In the output-error (OE) approach, the model parameters are optimized to match the modeled outputs to measured output data. The model outputs are computed by simulating the model with measured input data. Measurement noise is assumed on the measured output data, but process noise and model structure error are neglected. Using Fourier transform data, rather than time history samples, the model residuals are the output errors

$$\boldsymbol{\nu}(j\omega_k) = \mathbf{z}(j\omega_k) - \mathbf{y}(j\omega_k) \tag{18}$$

where $\mathbf{z}$ are the measured output data. The cost function to be minimized is

$$J(\boldsymbol{\theta}, \mathbf{S}_{\nu\nu}) = M \sum_{k=1}^{M} \boldsymbol{\nu}^{\dagger}(j\omega_k)\, \mathbf{S}_{\nu\nu}^{-1}\, \boldsymbol{\nu}(j\omega_k) + M \ln |\mathbf{S}_{\nu\nu}| \tag{19}$$

where M is the number of frequency points analyzed and $\mathbf{S}_{\nu\nu}$ is the spectral density of $\boldsymbol{\nu}(t)$. The cost function is alternately optimized with respect to $\boldsymbol{\theta}$ and $\mathbf{S}_{\nu\nu}$ while holding the other constant. The optimization with respect to $\mathbf{S}_{\nu\nu}$ is analytical, whereas the optimization with respect to $\boldsymbol{\theta}$ is nonlinear and involves iterations, for example using the Gauss-Newton method.

Output error was used first because it could be applied to the aeroelastic estimation problem directly and without modification. Formulated in the frequency domain, the analysis was tailored to the specific frequency bands excited by the inputs. The SIDPAC function `fdoe.m` was used to run the parameter estimation. Because the input pairwise correlations were low, as discussed in Section V, no detrimental effects to the parameter estimation were expected from identifying bare-airframe dynamics from closed-loop data.

The most difficult part of the output-error analysis was the model structure determination. Because linear models were desired, choosing the model structure involved picking the modes to include in the model and the stability and control derivatives to estimate. Model structure determination was applied in a trial-and-error approach until parameter estimates began to resemble reasonable values as compared to the ZAERO^{TM} predictions. Helpful simplifications included using only longitudinal excitations and beginning with lower bandwidth inputs, although this led to slightly biased parameters, as discussed in Section VI.B.

Compounding the model structure problem was the amount of time needed to solve the optimization. One reason for the high amount of computation time was the large number of model parameters to be determined. For every iteration of the optimization, a large model is assembled, sensitivity functions are computed for each parameter using finite differences, and the equations of motion are solved. At one point, programming analytical sensitivity equations [10] was considered, but additional insight from other methods improved the model structure and led to faster convergence times. Other methods for temporarily speeding up the computations included using decoupled maneuvers to reduce the model order, improving the efficiency of the code, limiting the frequency points to those in the multisine inputs, reducing the number of outputs, and lowering the finite difference order. A recursive technique [27] for computing the model output

$$\mathbf{y}(j\omega_k) = \left[\mathbf{C}\left(j\omega_k \mathbb{I} - \mathbf{A}\right)^{-1}\mathbf{B} + \mathbf{D}\right]\mathbf{u}(j\omega_k) \tag{20}$$

was also implemented to avoid computing the full matrix inverse at every frequency. It was found that this method was slower than the native MATLAB® routines, and was only faster than the SIDPAC code `misvd.m` for systems up to 5^{th} order, and was therefore abandoned in this work. Still, using output error in the frequency domain was significantly faster than using time domain data because fewer modeling points are used, fewer parameters are estimated, and the equations of motion are solved using linear algebra rather than numerical integration.

It was found that time delays could not be identified simultaneously with the stability and control derivatives from the initial starting values of the model parameters. Similar situations are described by Refs. [23, 26]. A successful approach was to first converge on values of the stability and control derivatives, then to restart the optimization while estimating both the time delays and the stability and control derivatives.

An example fit result to Fourier transform data is shown in Fig. 14. Although more outputs were matched during the estimation, only the match to a_z^{soa} is shown here, for clarity. The data appear jagged because of the spacing of the discrete analysis frequencies. Both the magnitude and phase of the Fourier transform were matched well over the modeling bandwidth, which included the SP and SW1B modes. These plots were representative of other results for matching gyroscope and accelerometer data. More information on identified models of the X-56A using the output-error approach with Fourier transform data can be found in Ref. [10], including accurate identification of the aeroelastic flutter mechanism.

B. Frequency Response Error

A related approach was frequency response error (FRE). In this approach, the matrix of frequency responses from input to output pairs is first computed from the measured data, and then the parameters are estimated that best match the model frequency response to the empirical frequency response data. In this case, the model residuals are

$$\boldsymbol{\nu}(j\omega_k) = \mathrm{vec}\left[\mathbf{H}(j\omega_k)\right] - \mathrm{vec}\left[\hat{\mathbf{H}}(j\omega_k)\right] \tag{21}$$

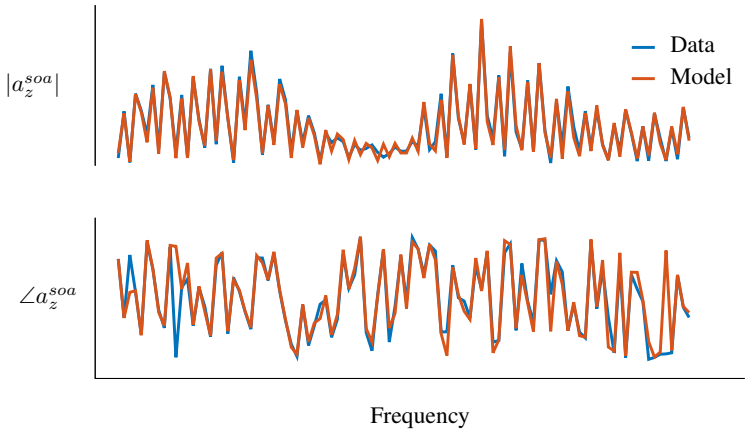

Fig. 14 Output-error fit to accelerometer Fourier transform data (Flight 11, FTA 503, $0.63V_f$, $0.48w_{ff}$).

where $\mathbf{H}(j\omega_k)$ is the measured frequency response data, $\hat{\mathbf{H}}(j\omega_k)$ is the model frequency response, and vec is an operator that stacks elements of a matrix into a column vector. The cost function for this case is, similar to Eq. (19),

$$J(\boldsymbol{\theta}, \mathbf{S}_{\nu\nu}) = M \sum_{k \in K} \boldsymbol{\nu}^{\dagger}(j\omega_k)\, \mathbf{S}_{\nu\nu}^{-1}\, \boldsymbol{\nu}(j\omega_k) + M \ln |\mathbf{S}_{\nu\nu}| \tag{22}$$

where here $\mathbf{S}_{\nu\nu}$ represents the spectral density of the frequency response errors and M is the number of multisine harmonic frequencies. The optimization was also performed using the SIDPAC function `fdoe.m`, but the subroutine `estsvv.m` was modified to allow for fully-populated spectral density matrices [9].

The multisine inputs facilitated a simple way of computing the frequency responses. For open-loop systems, the frequency responses are ratios of the output and input data at the harmonic frequencies [14, 28]. The X-56A included mixing of the control surfaces and feedback control, so harmonic frequencies were not unique to a particular input. A procedure was developed in Ref. [11] using linear interpolation to account for the frequency correlation and to successfully compute frequency responses of bare-airframe dynamics from closed-loop data. The entire frequency response matrix could be computed from a single maneuver using this technique because all control surfaces were excited. The use of frequency responses was helpful in verifying predictive models and gaining insight into the dynamics and model structure. The main drawback for this approach was that a separate step was needed to obtain the modeling data from the measured data, beyond the Fourier transform. However, the computations were simple, straightforward to do, and did not require much computation time.

Although for most maneuvers only one period of the multisine was applied, some maneuvers contained 2 or 3 cycles of the input. In previous work, it was suggested that integer periods of excitation should be used to obtain the most accurate results because of partial-period Fourier transform errors [28]. It was found here that if the maneuver only included one period of the excitation input, it was better to include the trim data before and after the excitation, if available. The reason is that transient responses occurring after the excitation starts, which degrade frequency response estimates near the resonant frequencies, are to a large extent cancelled by the transient responses occurring when the excitation stops. However, if the data contains multiple periods of the excitation, it is still more accurate to discard the first period of the input, which may contain transients, and only use the remaining integer periods of data for computing frequency responses.

Working with frequency responses was helpful. One benefit was that the model frequency responses can be computed without solving the equations of motion, which reduced computational requirements during the iterative optimization. Frequency responses also facilitated using simpler models for parameter estimation. For example, a single input could be initially considered during the parameter estimation to reduce the number of control derivatives estimated and to focus on choosing which stability derivatives to estimate. Drawbacks of using frequency responses are that models are restricted to LTI systems and errors can be introduced when frequency responses are computed if signal-to-noise ratios are low or if there is atmospheric turbulence present.

An example result for fitting frequency response data is shown in Fig. 15. Many frequency responses were used in the modeling but only the a_z^{soa}/δ_{wf4s} is shown here, for clarity. The dots are the frequency response data, which were computed at the harmonic frequencies included in the δ_{wf4s} multisine. The solid line is the frequency response of the

identified model. These results fit the data well over the modeling bandwidth, which included the SP and SW1B modes, and was representative of other results. Additional discussion of results using this approach and comparisons with the OE approach is found in Refs. [11, 12].

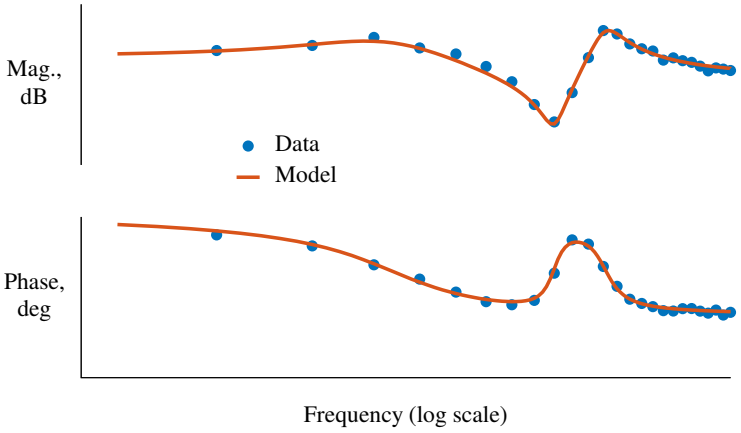

Fig. 15 Frequency response error fit to a_z^{soa}/δ_{wf4s} (Flight 11, FTA 503, 0.63V_f, 0.48w_{ff}).

C. Equation Error

In the equation-error (EE) approach, model parameters are optimized that match data for each aerodynamic coefficient with a model for that coefficient. The model residual is

$$\nu(j\omega_k) = C_a(j\omega_k) - \mathbf{x}^T(j\omega_k)\boldsymbol{\theta} \tag{23}$$

where C_a is a nondimensional aerodynamic coefficient and here $\mathbf{x}$ is a complex-valued regressor vector containing Fourier transforms of measured explanatory variables. Each row of Eq. (11) can be arranged in this way for the nondimensional coefficients. The estimation problem is decoupled in that each aerodynamic coefficient is modeled separately. The cost function in this case is

$$J(\boldsymbol{\theta}) = \sum_{k=1}^{M} \nu(j\omega_k)^\dagger \nu(j\omega_k) \tag{24}$$

and is only a function of $\boldsymbol{\theta}$ because of the decoupling. The solution to this least-squares problem is analytical, fast to compute, and does not require iteration. Another benefit is that automated techniques for model structure determination can be leveraged to select which stability and control derivatives should be retained in the model [14].

Despite these advantages, an EE analysis was not initially possible because measurements of η_k and $\dot{\eta}_k$ were not available, and because the sensor measurements contained additional contributions from the aircraft vibration, per Eq. (17) and as detailed in Ref. [8]. However, Ref. [7] introduced a technique for reconstructing the required information from the measurements and FEM/GVT data. The idea was to exploit redundant data to separate contributions to the sensor measurements from rigid-body and elastic sources. Specifically, accelerometers were used to obtain C_X, C_Y, C_Z, and $\ddot{\eta}_k$; airdata and gyroscopes were used to obtain V, α, β, p, q, r, and $\dot{\eta}_k$; and strain gauges and attitude data were used to obtain ϕ, θ, ψ, and η_k. Because the structural displacements, rates, and accelerations are kinematically related, a Kalman filter was also used to fuse this information and improve estimates of the structural motion, which was then used to compute C_{Q_i}. Given this information, estimation using the EE approach could proceed normally using the SIDPAC routine `lesq.m` for batch estimation or `rtpid.m` for real-time estimation. The codes `mof.m` and `swr.m` were used for model structure determination using multivariate orthogonal functions and step-wise regression, respectively.

The primary cost for using the EE method with reconstructed data is the amount of care and effort needed to ensure the reconstructed data are accurate. The frequency-domain analysis provides robustness to high-frequency noise because that content is automatically removed from the data during the Fourier transform. For aeroelastic analysis, the EE method also benefits from many redundant sensors which improve the modeling data. However, the number of structural states that can be reconstructed using this technique is limited by the number of sensor redundancies.

An example result of fitting nondimensional coefficients using the EE method is shown in Fig. 16. Data from all 18 accelerometers were combined with a least squares estimator to produce Fig. 16(a), which shows the reconstructed C_Z and $\ddot{\eta}_7$ time histories. Uncertainties were also available for these time histories, but are not shown here for clarity. The C_Z data contain mostly slower rigid-body motions, whereas the $\ddot{\eta}_7$ data contain oscillations at the faster SW1B resonant frequency. Fits to Fourier transform absolute values for the nondimensional aerodynamic coefficients are shown in Fig. 16(b) and were very close to the measured data. Only small differences at the lowest frequencies, perhaps due to phugoid motion, were visible in C_L and C_{Q_7}. A 4^{th}-order model involving the SP and SW1B modes was estimated, and all stability and control derivatives were significant except for C_{L_q}, which is common for tailless airplanes.

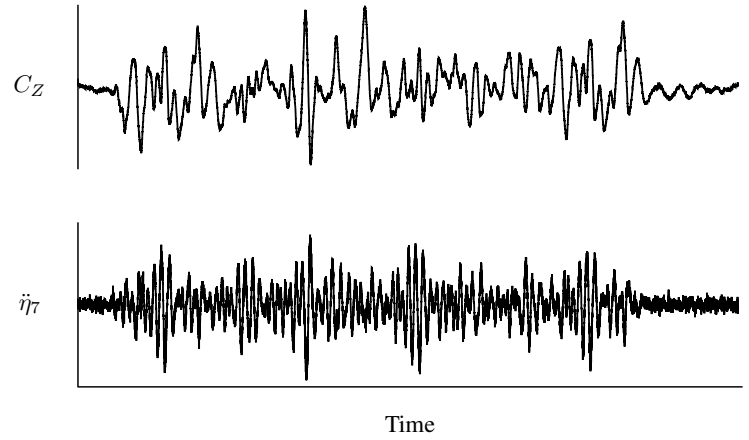

(a) Reconstructed time histories.

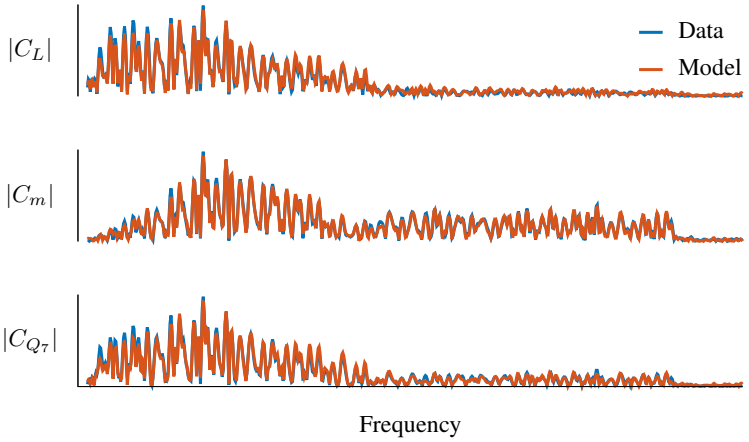

(b) Fits to modeling data.

Fig. 16 Equation-error results (Flight 16, FTA 503, 0.73V_f, 0.63w_{ff}).

D. Further Discussion

Each of the three methods for parameter estimation were based on maximum likelihood estimation, which has favorable theoretical properties such as asymptotically unbiased estimates and accurate parameter uncertainties without correction factors. These estimators were successfully applied to estimating aerodynamic models of the bare-airframe dynamics from flight test data measured during flight tests under feedback control and mixing of the control surfaces. Most of the estimates obtained from these three methods were in good agreement. For example, a comparison of pitching moment control derivatives are shown in Fig. 17 for each of the three parameter estimation methods, as well as additional estimates from wind tunnel tests with a half-span model and from using ZAERO^{TM}. The estimates obtained from flight test were mutually consistent, and were in better agreement than results obtained from the wind tunnel and

numerical analysis. In addition to the estimated values, the parameter estimation also yielded uncertainties on the parameter estimates, which are shown in Fig. 17 as ±2 standard errors.

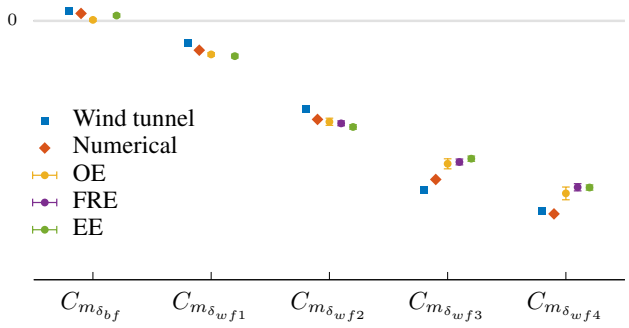

Fig. 17 Control derivative estimates (Flight 11, FTA 506, $0.65V_f$, $0.29w_{ff}$).

All the parameter estimation methods were applied to data in the frequency domain, which was a significant advantage over using time-domain methods [6]. Because the multisines were designed to have a specific frequency bandwidth, the parameter estimation was also restricted to that bandwidth, resulting in fewer data points to process and more efficient computations using linear algebra rather than numerical integration. Selecting the modeling bandwidth automatically removed high-frequency noise and unmodeled structural dynamics. Furthermore, the estimation problem was simplified in the frequency domain because additional bias parameters were unnecessary. It was noted in Ref. [6] that the output-error analysis was more sensitive to initial conditions when using time-domain data, rather than Fourier transform data, perhaps because of the increased number of parameters to estimate. Frequency domain analysis also facilitated a simple way of including time delays and sensor or filter dynamics with the measurements. In the time domain, time delays are restricted to integer multiples of the sampling period or interpolations are required, and filter dynamics further increase the model order.

The estimation techniques had different advantages and disadvantages. The OE and FRE approaches were iterative, which required good starting values for the model parameters and additional time over the equation-error method for obtaining convergence. It also was cumbersome to determine which stability and control derivatives to estimate, which was done by trial and error. In contrast, the EE approach had an analytical solution that could be computed quickly and in real time, and enabled statistical tests for automatically selecting which parameters to retain in the model. Furthermore, changing the code for different model structures was trivial. In the OE and FRE methods, much more data could be matched directly by the estimator to potentially improve the estimation accuracy, but this feature also increased the complexity of the estimation problem and the amount of computation time needed. Overall, it was helpful to use a variety of modeling techniques for this problem to gain insight into the problem and develop confidence in the results.

In comparison to the OE approach, which directly matched measured output data, the FRE and EE approaches required further processing of the data before modeling. Bode plots were computed for FRE, whereas dependent and explanatory modeling variables were computed for EE. These extra steps introduced opportunities for errors in the modeling data. For example with FRE, Bode plots could not be accurately computed from the δ_{bfs} and δ_{wf1s} inputs due to low signal-to-noise ratios. This could have been due to reduced effectiveness from the thicker fuselage cross section or interference with the propulsion system. However, good estimates were obtained using OE and EE. More accurate Bode plots could have been produced by increasing the multisine amplitudes for these inputs. The benefit of the extra processing steps is additional insight into the data, whether by observing the Bode plots between input-output pairs using FRE, or by having access to the direct aerodynamic forces and moments being modeled using EE.

The OE and FRE methods were implemented with a Gauss-Newton method which is sensitive to starting values for the model parameters. When choosing starting values for the model parameters, it was more efficient to take the estimates from ZAERO^{TM} and residualize the system, rather than to use the estimates directly. For example, when estimating a rigid-body dynamics model, the OE approach converged in 45 iterations from parameters originally produced by the ZAERO^{TM} model. When the structural modes in that model were residualized, as in Fig. 13, and the augmented stability and control derivatives were used as starting values for the optimization, convergence (to the same parameters) was obtained after 30 iterations. Therefore, the residualized stability and control derivatives from a simulation model should be used to start the optimization if results are not available from an EE analysis.

Figure 18 shows a plot matrix of the data used for modeling the short period and SW1B mode in an EE analysis, similar to Fig. 9(a). The modeling terms have low pairwise correlation coefficients, all under about 0.5 in absolute value, which did not pose a problem for the modeling step. The data can become correlated if the excitation does not extend through the structural frequencies of interest, in which case the structural modes are excited through the coupling in the system dynamics. However, here the multisines covered the structural modes and the modeling data were sufficiently decorrelated for accurate modeling.

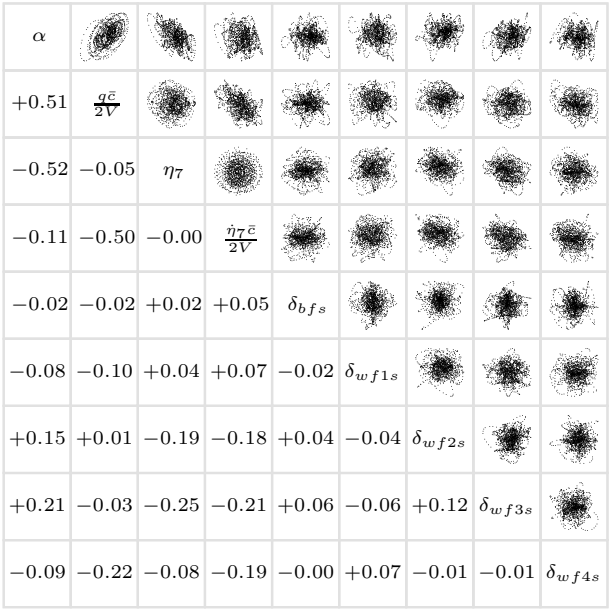

Fig. 18 Correlation cross plots of modeling data (Flight 11, FTA 506, $0.65V_f$, $0.29w_{ff}$).

Parameter estimation was significantly easier for flight conditions at low speeds relative to the open-loop flutter speed. This was in part because additional structural modes, more modeling complexity, and more accurate starting values for model parameters were needed to obtain convergence, as mentioned previously in Section VI.B. Because nondimensional parameters were identified, these models could predict the aeroelastic flutter instability even though parameter estimates were identified from low-speed data [10].

As mentioned in Section IV, some filters and sensors had appreciable dynamics relative to the aeroelastic modes of interest. It was found that including these dynamics in the parameter estimation was important for obtaining accurate results. Although the Bode magnitudes were not significantly affected through the modeling bandwidth, there were large Bode phase distortions due to the large filter orders. If these dynamics were not included, the parameters that are more difficult to identify accurately, such as C_{m_q}, would degrade in accuracy.

In testing of flexible aircraft, the structural modes, frequencies, and damping ratios are not always known before a flight test. During the identification analysis, elements of the $\mathbf{A}_{ee}$ matrix in Eq. (15a) become confounded, and instead the equivalent frequency and damping ratios are estimated from the relations [17, 18]

$$-\omega_{i_{eq}}^2 = \frac{\bar{q}S\bar{c}}{m_i} C_{Q_{i_{\eta_i}}} - \omega_i^2 \tag{25a}$$

$$-2\zeta_{i_{eq}}\omega_{i_{eq}} = \frac{\bar{q}S\bar{c}}{m_i}\frac{\bar{c}}{2V} C_{Q_{i_{\dot{\eta}_i}}} - 2\zeta_i\omega_i \tag{25b}$$

It is typical to set the generalized masses equal to unity. The mode shape contributions in the output equations can be estimated up to a constant, meaning that all but one of the mode shape constants can be estimated. This estimation needs to be done at every flight condition. However, if this is done for multiple dynamic pressures, the structural frequencies and damping ratios can be ascertained. Using information from an accurate FEM/GVT helps to reduce the modeling problem and provide better insight into the aeroelastic flight dynamics.

IX. Conclusions

This paper summarized practical aspects and lessons learned for the system identification of the X-56A MUTT during the Phase 1 flight tests conducted at NASA AFRC from 2017–2019. Due to the level of structural flexibility in the X-56A design and the aeroelastic instability within the normal flight envelope, a number of unique challenges were encountered during the system identification analysis.

The main findings from analyzing the X-56A Phase 1 flight tests are discussed throughout the paper. A few broad conclusions are the following:

1) Fully-coupled aeroelastic flight dynamics models are significantly more complicated than rigid-body models, and require high quality instrumentation and efficient record keeping of flight parameters.
2) Orthogonal phase-optimized multisine inputs, added to command path at the actuators, provided excellent modeling data for the identification of the bare-airframe aeroelastic flight dynamics from experimental data with a control law and mixer active.
3) An accurate model of the vibration dynamics is helpful for experiment design, prior simulation testing, insight into critical modes, and reducing the number of unknown parameters in the estimation problem.
4) A frequency-domain approach to modeling is preferable for reducing the model complexity and for increasing accuracy and computational efficiency. Using a variety of frequency-domain methods is useful to gain confidence in estimation results and aid model structure determination.
5) Although it required the reconstruction of modeling variables from measured data, the equation-error approach significantly reduced computation times and enabled an automated approach for determining which stability and control derivatives to estimate. These approach avoided the two most difficult aspects of using the output error method and the frequency response error method with aeroelastic flight dynamic models.

Acknowledgments

This research was supported by the NASA Advanced Air Transport Technology (AATT) Project. The efforts of the X-56A team at NASA Armstrong Flight Research Center (AFRC) are gratefully acknowledged. In particular, conversations with and analyses provided by Alex Chin, Christopher Miller, Jeffrey Ouellette, Jacob Schaefer, Peter Suh, and other X-56A team members were significant. Additional technical conversations with David Schmidt are acknowledged and appreciated.

References

[1] Beranek, J., Nicolai, L., Buonanno, M., Burnett, E., Atkinson, C., Holm-Hansen, B., and Flick, P., "Conceptual Design of a Multi-Utility Aeroelastic Demonstrator," AIAA Paper 2010-9350, 2010. doi:10.2514/6.2010-9350.

[2] Ryan, J., Bosworth, J., and Burken, J., "Current and Future Research in Active Control of Lightweight, Flexible Structures Using the X-56," AIAA Paper 2014-0597, 2014. doi:10.2514/6.2014-0597.

[3] Levine, J., "X-56A Suppresses Flutter With Two Controllers," `http://nasa.gov`, Nov. 28, 2018.

[4] Schmidt, D., *Modern Flight Dynamics*, McGraw Hill, New York, NY, 2012.

[5] McRuer, D., Ashkenas, I., and Graham, D., *Aircraft Dynamics and Automatic Control*, Princeton University Press, Princeton, NJ, 1973.

[6] Grauer, J., and Boucher, M., "Aeroelastic Modeling of X-56A Stiff-Wing Configuration Flight Test Data," AIAA Paper 2017-0699, 2010. doi:10.2514/6.2017-0699.

[7] Grauer, J., and Boucher, M., "Real-Time Parameter Estimation for Flexible Aircraft," AIAA Paper 2018-3155, 2018. doi:10.2514/6.2018-3155.

[8] Grauer, J., and Boucher, M., "Output Measurement Equations for Flexible Aircraft Flight Dynamics," NASA TM-220102, Oct. 2018.

[9] Grauer, J., "Dynamic Modeling using Output-Error Parameter Estimation based on Frequency Responses Estimated with Multisine Inputs," NASA TM-220108, Nov. 2018.

[10] Grauer, J., and Boucher, M., "Identification of Aeroelastic Models for the X-56A Longitudinal Dynamics Using Multisine Inputs and Output Error in the Frequency Domain," *Aerospace*, Vol. 24, No. 6, 2019, pp. 1–25. doi:10.3390/aerospace6020024.

[11] Grauer, J., and Boucher, M., "Real-Time Estimation of Bare-Airframe Frequency Responses from Closed-Loop Data and Multisine Inputs," *Journal of Guidance, Control, and Dynamics*, 2019. doi:10.2514/1.G004574.

[12] Grauer, J., and Boucher, M., "Aircraft System Identification from Multisine Inputs and Frequency Responses," AIAA Paper to be published, 2020.

[13] Morelli, E., "System IDentification Programs for AirCraft (SIDPAC)," version 4.1, NASA Software Catalog, `http://software.nasa.gov`, accessed Nov. 2019.

[14] Morelli, E., and Klein, V., *Aircraft System Identification: Theory and Practice*, Sunflyte Enterprises, Williamsburg, VA, 2016.

[15] Pak, C., and Truong, S., "Creating a Test-Validated Finite-Element Model of the X-56A Aircraft Structure," *Journal of Aircraft*, Vol. 52, No. 5, 2015, pp. 1644–1677. doi:10.2514/1.C033043.

[16] Ouellette, J., "Aeroservoelastic Modeling of Body Freedom Flutter for Control Systen Design," AIAA Paper 2017-0019, 2017. doi:10.2514/6.2017-0019.

[17] Theodore, C., Ivler, C., Tischler, M., Field, E., Neville, R., and Ross, H., "System Identification of Large Flexible Transport Aircraft," AIAA Paper 2008-6894, 2008. doi:10.2514/6.2008-6894.

[18] Silva, B., and M onnich, W., "System Identification of Flexible Aircraft in Time Domain," AIAA Paper 2012-4412, 2012. doi:10.2514/6.2012-4412.

[19] Heeg, J., and Morelli, E., "Evaluation of Simultaneous Multisine Excitation of the Joined Wing SensorCraft Aeroelastic Wind Tunnel Model," AIAA Paper 2011-1959, 2011. doi:10.2514/6.2011-1959.

[20] Milne, R., "Dynamics of the Deformable Aeroplane," Aeronautical Research Council No. 3345, Sep. 1964.

[21] Waszak, M., and Schmidt, D., "Flight Dynamics of Aeroelastic Vehicles," *Journal of Aircraft*, Vol. 25, No. 6, 1988, pp. 563–571. doi:10.2514/3.45623.

[22] McLean, D., *Automatic Flight Control Systems*, Prentice Hall, Englewood Cliffs, NJ, 1990.

[23] Tischler, M., and Remple, R., *Aircraft and Rotorcraft System Identification: Engineering Methods with Flight Test Examples*, 2nd ed., AIAA, Reston, VA, 2012. doi:10.2514/4.868207.

[24] Schmidt, D., "MATLAB-Based Flight-Dynamics and Flutter Modeling of a Flexible Flying-Wing Research Drone," *Journal of Aircraft*, Vol. 53, No. 4, 2016, pp. 1045–1055. doi:10.2514/1.C033539.

[25] Steers, S., and Iliff, K., "Effects of Time-Shifted Data on Flight-Determined Stability and Control Derivatives," NASA TN D-7830, Mar. 1975.

[26] Morelli, E., "Dynamic Modeling from Flight Data with Unknown Time Skews," *Journal of Guidance, Control, and Dynamics*, Vol. 40, No. 8, 2017, pp. 2083–2091. doi:10.2514/1.G002008.

[27] Miller, K., "On the Inverse of the Sum of Matrices," *Mathematics Magazine*, Vol. 54, No. 2, 1981, pp. 67–72. doi: 10.2307/2690437.

[28] Grauer, J., and Morelli, E., "Method for Real-Time Frequency Response and Uncertainty Estimation," *Journal of Guidance, Control, and Dynamics*, Vol. 37, No. 1, 2014, pp. 336–343. doi:10.2514/1.60795.